J. Fluid Mech. (2000), *vol.* 416, *pp.* 117–149. Printed in the United Kingdom

© 2000 Cambridge University Press

Passive-scalar wake behind a line source in grid turbulence

By D. LIVESCU, F. A. JABERI† AND C. K. MADNIA

Department of Mechanical and Aerospace Engineering,
State University of New York at Buffalo, Buffalo, NY 14260, USA

(Received 6 May 1999 and in revised form 6 March 2000)

The structure and development of the scalar wake produced by a single line source are studied in decaying isotropic turbulence. The incompressible Navier–Stokes and the passive-scalar transport equations are solved via direct numerical simulations (DNS). The velocity and the scalar fields are generated by simulating Warhaft's (1984) experiment. The results for mean and r.m.s. scalar statistics are in good agreement with those obtained from the experiment. The structure of the scalar wake is examined first. At initial times, most of the contribution to the scalar variance is due to the flapping of the wake around the centreline. Near the end of the turbulent convective regime, the wake develops internal structure and the contribution of the flapping component to the scalar variance becomes negligible. The influence of the source size on the development of the scalar wake has been examined for source sizes ranging from the Kolmogorov microscale to the integral scale. After an initial development time, the half-widths of mean and scalar r.m.s. wakes grow at rates independent of the source size. The mixing in the scalar wake is studied by analysing the evolution of the terms in the transport equations for mean, scalar flux, variance, and scalar dissipation. The DNS results are used to test two types of closures for the mean and the scalar variance equations. For the time range simulated, the gradient diffusion model for the scalar flux and the commonly used scalar dissipation model are not supported by the DNS data. On the other hand, the model based on the unconditional probability density function (PDF) method predicts the scalar flux reasonably well near the end of the turbulent convective regime for the highest Reynolds number examined. The scalar source size does not significantly influence the models' predictions, although it appears that the time-scale ratio of mechanical dissipation to scalar dissipation approaches an asymptotic value earlier for larger source sizes.

1. Introduction

A better understanding of the diffusion of passive scalars in turbulent flows has important applications in engineering, atmospheric and oceanic sciences. Some examples are improving the mixing efficiency in combustion devices, the dispersion of pollutants in the atmosphere, and salinity and temperature fluctuations in the oceans. With the current capabilities of computers, the DNS of practical flows is not feasible, and measurements of these flows are extremely difficult (Givi 1994). Some features of the mixing and dispersion rates of scalar contaminants in turbulent flows are likely to be understood by studying the passive-scalar wake behind a line source in homogeneous

† Present address: Department of Mechanical and Nuclear Engineering, Kansas State University, Manhattan, KS 66506-5205, USA.

https://doi.org/10.1017/S0022112000008910 Published online by Cambridge University Press

turbulence. This problem is also of fundamental interest, being the first step toward understanding more complicated aspects of the dynamics of turbulent mixing and reaction. Theoretical studies were done as long as sixty years ago (Taylor 1935), but the problem still remains unsolved from a fundamental point of view. One of the difficulties in modelling the scalar wake is that the length scale of the scalar field is different from that of the turbulence during the initial stages of the wake development. This is also the reason for the failure of gradient-like models in simulating the turbulent wake (Anand & Pope 1985).

In order to overcome this difficulty, more sophisticated models have been proposed. The probability density function (PDF) models (Pope 1985; Anand & Pope 1985) and the Lagrangian stochastic models based on two-point displacement (Durbin 1980; extended by Sawford & Hunt 1986 and Thomson 1990) predict well the experimental results for the mean statistics of the scalar wake and the normalized scalar variance profiles. However, the time evolution of other statistics such as the scalar intensity (the ratio of r.m.s. scalar to mean scalar) and the width of the r.m.s. scalar wake are still not well predicted. The classical phenomenology can be used to describe the scalar r.m.s. statistics (Thomson 1996), but it is limited to obtaining results in a number of distinct regimes and not in the transition between these regimes. Simpler models using shape parameters and assumptions about the similarity of the scalar field have also been proposed for the scalar r.m.s. and the higher-order moments (Chatwin & Sullivan 1990; Sawford & Sullivan 1995; Mole & Clark 1996). Although there are models that address some of the issues related to the source size dependence of the scalar wake (e.g. Sawford & Hunt 1986), they have not been tested for large source sizes, primarily due to the lack of experimental results.

Experiments on the dispersion of a scalar field downstream of a line source were carried out by Uberoi & Corrsin (1952), Townsend (1954), Warhaft (1984), and Stapountzis *et al.*(1986) using a small temperature difference as a passive scalar. Li & Bilger (1996) measured the reactive scalars in a chemically reactive plume behind a line source from which they extracted results for the conserved scalar. They also showed that these results are consistent with those measured in passive thermal plumes. In order to generate various initial profiles of mean and fluctuating temperature, experiments have been conducted using groups of heated wires (Warhaft & Lumley 1978; Sreenivasan *et al.* 1980). Although the temperature generated by an array of wires can be treated as a random initial temperature field, these results can also be explained by using the superposition of multiple line sources (Warhaft 1984). Important aspects of the first two moments of the passive scalar field have been elucidated using the experimental data. However, higher-order statistics of the scalar field are increasingly difficult to obtain experimentally, although significant steps have been taken recently in improving the accuracy and resolution of the measurements (Buch & Dahm 1996, 1998). There are also concerns about the homogeneity and isotropy of the velocity field and the passiveness of the scalar field.

Since many of the important scalar statistics are difficult to obtain experimentally, DNS has become an important tool in complementing experimental investigations of turbulent mixing. Although there are severe limitations to the capability of DNS in capturing the physics of the scalar mixing in high Reynolds number turbulence, there are certain advantages in its implementation for simulations at moderate and low Reynolds numbers (Givi 1989). DNS allows the researcher a degree of control in isolating specific physical phenomena that are almost inaccessible in experiments. The characteristics of the scalar small-scale structures, the behaviour of the scalar spectra, and higher-order moments of the scalar field can thus be analysed in great

https://doi.org/10.1017/S0022112000008910 Published online by Cambridge University Press

detail (Kerr 1985; Ruetsch & Maxey 1991; Leonard & Hill 1991; Miller *et al.* 1995; Jaberi *et al.* 1996; Overholt & Pope 1996). Recent advances in supercomputer capabilities and algorithms make it possible, by performing DNS, to simulate the laboratory experiments on turbulent mixing processes. A successful confirmation of the experimental results will lend confidence to future numerical results.

The main goals of the present paper are: (1) to examine the structure and development of the scalar wake behind a line source in isotropic turbulence, (2) to study the influence of the source size ranging from the Kolmogorov microscale to the integral scale and (3) to assess the behaviour of the gradient-diffusion-type models and PDF models. Several runs have been performed, including the simulation of the velocity and scalar fields from Warhaft's (1984) experiment.

This paper is organized as follows. Section 2 contains the governing equations and the numerical methodology. Characteristics of the velocity field are presented in § 3. The results pertaining to the scalar field are discussed in § 4. In § 4.1 the DNS results for the scalar field statistics are compared to the experimental ones. Also in this section, the structure of the scalar wake produced by a thin scalar source is discussed. In § 4.2, the influence of the source size on the mean and r.m.s. scalar wake and on the structure of the wake is examined. The mechanisms which contribute to the spreading of the wake are studied in § 4.3 by analysing the variation of each term in the transport equations for mean scalar, scalar flux, scalar variance and scalar dissipation. Also in this section, two types of closures for the mean scalar and scalar variance equations are assessed via numerical data. Summary and conclusions are stated in § 5.

2. Formulation and numerical methodology

2.1. *Flow configuration and basic assumptions*

Direct numerical simulations of the mixing of a passive scalar field produced by a single line source in decaying isotropic turbulence were conducted, and the results are compared with Warhaft's (1984) experiment for a single line source (referred to hereinafter as W84). In order to better understand the numerical approach, a brief description of the W84 experiment is provided. In the first part of the experiment, detailed measurements of the mean and variance of the thermal wake behind a single line source in grid turbulence were performed (figure 1). The wire is placed perpendicular to the mean velocity U, in the z-direction. The diameter d of the wire is smaller than the Kolmogorov microscale in order to minimize its effect on the velocity field. The excess temperature was small enough for the temperature to be considered a passive scalar. The distance from the grid to the heated wire is x_0 and the distance from the heated wire to the measurement plane is x'. M is the mesh length of the turbulence-generating grid. Numerical values for the experimental set-up with which we compare our results are: $U = 7\,\mathrm{m\,s^{-1}}$, $M = 0.025\,\mathrm{m}$, $x_0/M = 52$, $d = 0.025\,\mathrm{mm}$ ($\approx 0.07\eta_K$) for measurements up to $x'/M = 8.1$ and $d = 0.127$ mm ($\approx 0.36\eta_K$) for measurements beyond $x'/M = 8.1$, where η_K is the Kolmogorov microscale.

In our numerical simulations of the W84 experiment, we employ the Taylor transformation (Townsend 1954; Anand & Pope 1985; Stapountzis *et al.* 1986) approximating the continuous line source from the experiment with an instantaneous plane source. The experimental thermal wake statistics at x' and y are similar to those at t and y for the plane source, where $t = x'/U$. The approximation is valid as long as the turbulence intensity $\langle u^2\rangle^{1/2}/U$ is small and the mean axial gradients are small compared with lateral gradients, conditions satisfied by the W84 experiment. Consistent with Taylor

https://doi.org/10.1017/S0022112000008910 Published online by Cambridge University Press

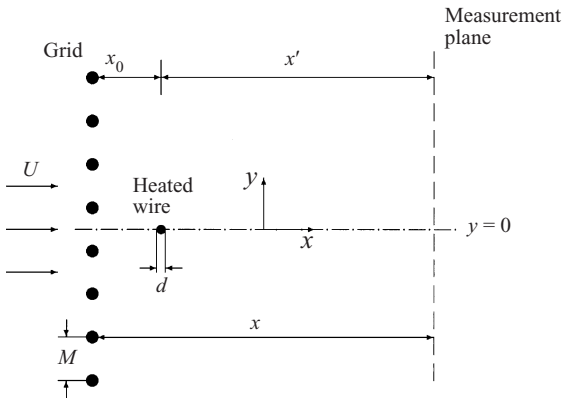


FIGURE 1. Typical experimental set-up for passive scalar measurements from a single line source in grid turbulence.

transformation, the scalar field is initialized in DNS with non-zero values in a slab perpendicular to the y-axis and zero elsewhere. The resulting scalar field is homogeneous in the x- and z-directions and inhomogeneous in the y-direction. The simulation is stopped before the scalar wake reaches the boundaries of the computational domain.

2.2. *Governing equations*

The equations solved are the non-dimensionalized Navier–Stokes equations and the transport equation for the passive scalar. The flow is assumed to be homogeneous, isotropic and incompressible:

$$\frac{\partial u_j}{\partial x_j} = 0, \tag{2.1}$$

$$\frac{\partial u_i}{\partial t} + \frac{\partial (u_i u_j)}{\partial x_j} = -\frac{\partial p}{\partial x_i} + \frac{1}{Re_0}\frac{\partial^2 u_i}{\partial x_j \partial x_j}, \tag{2.2}$$

$$\frac{\partial Y}{\partial t} + \frac{\partial (u_j Y)}{\partial x_j} = \frac{1}{Re_0 Sc}\frac{\partial^2 Y}{\partial x_j \partial x_j}. \tag{2.3}$$

The independent variables are the velocity u_i, the pressure p and the passive-scalar mass fraction Y. All the variables in the above equations are normalized using reference length (L_0) and velocity (u_0) scales. The passive scalar is scaled such as it takes values in the interval [0, 1]. The non-dimensional parameters in equations (2.2) and (2.3) are the Reynolds number, $Re_0 = u_0 l_0/\nu$, and the Schmidt number, $Sc = \nu/D$. The kinematic viscosity ν and the mass diffusivity D are assumed to be constant, resulting in $Sc = 0.72$.

The computational domain is a cubic box with 128^3 grid points. The reference frame is moving with constant velocity equal to the mean velocity of the flow. In this coordinate system the values of the mean velocities in all three directions are zero. The governing equations are integrated using the Fourier spectral-collocation method (Gottlieb & Orszag 1977; Givi & Madnia 1992; Givi 1994) with triply periodic boundary conditions. Time advancement is provided by a second-order-accurate Adams–Bashforth technique. Aliasing errors are controlled by removing the energy from the wavenumbers with magnitude over $\sqrt{2}N/3$. Since the scalar field is homogeneous in the directions x and z, all the averages involving the scalar mass fractions are defined over these directions, unless otherwise stated.

https://doi.org/10.1017/S0022112000008910 Published online by Cambridge University Press

	W84	DNS
L_{ref}	0.0135 m	0.8147
t_{ref}	0.0882 s	1.797
u_{ref}	0.153 m s^{-1}	0.4533

TABLE 1. Numerical values for the reference scales.

2.3. *Initial conditions*

The velocity field is initialized as a random solenoidal three-dimensional field with zero mean and Gaussian energy spectrum. The parameters which control the velocity field are the Reynolds number (Re_0) and the initial location of the peak of the energy spectrum (K_0).

In order to relate the numerical results to the experimental ones, reference scales are defined. The values of the Eulerian velocity integral scale ($L = (u_{rms}^2)^{3/2}/\epsilon$), r.m.s. velocity fluctuations (u_{rms}) and eddy turnover time ($\tau = u_{rms}^2/\epsilon$) at the location of the heated wire are chosen as the reference scales used for the non-dimensionalization of the experimental quantities. The reference scales for numerical simulations are defined as the DNS values of the Eulerian velocity integral scale, r.m.s. velocity fluctuations and eddy turnover time at the time t_0 corresponding to the location of the heated wire (table 1). The time t_0 is determined as when the value of the Reynolds number based on Taylor microscale (Re_λ) in numerical simulation matches the experimental value of Re_λ at the location of the heated wire. Knowing the reference scales, the non-dimensional time in the numerical simulation can be related to the distance from the heated wire in the experiment:

$$t' = t - t_0 = \frac{(t_{ref})_{DNS}}{(t_{ref})_{expt}} \frac{x'}{U}. \tag{2.4}$$

Using (2.4), the numerical times corresponding to the other experimental measurement points can be found. Various quantities pertaining to the velocity field can now be directly compared between the experiment and the DNS. The initial parameters of the velocity field (Re_0 and K_0) are chosen such that the values of Re_λ from numerical simulation and W84 matched at all the measurement points. The values obtained are $Re_0 = 350$ and $K_0 = 1.5$. The reference scales for both DNS and experiment are presented in table 1.

In order to verify that the flow is accurately simulated, the product of the highest wavenumber and the Kolmogorov length scale, $k_{max}\eta_K$, was calculated. The initial value of $k_{max}\eta_K$ is 1.55 and in the domain of interest ($t > t_0$) $1.28 < k_{max}\eta_K < 1.75$. Examination of the velocity energy spectra at different times (not shown here) also indicates that all wavenumbers are well resolved during the simulation.

In addition to the base velocity field, several other simulations were performed with values of the initial Reynolds number Re_0 between 100 and 350, resulting in Re_λ between 24 and 44 at the moment when the scalar field is initialized. Although it is difficult to draw conclusions about the high-Reynolds-number behaviour based on these simulations, they can provide information about the Reynolds number dependence of some of the quantities presented in the next sections. All the results presented in the subsequent sections were obtained using the base velocity field, unless otherwise stated.

https://doi.org/10.1017/S0022112000008910 Published online by Cambridge University Press

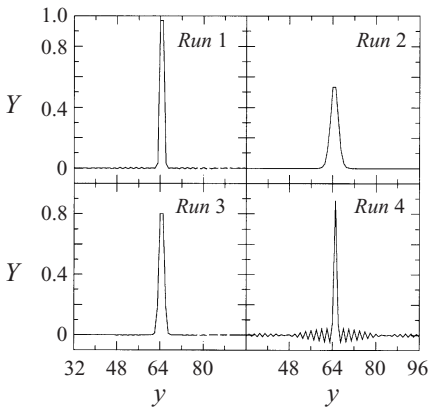


FIGURE 2. Initial scalar profiles; $y = 1$–128 represent the grid points.

As mentioned above, the scalar field is initialized with non-zero values in a slab perpendicular to the y-axis and zero elsewhere. This profile is Fourier transformed and the wavenumbers higher than k_{max} are discarded. The initial slab cannot be represented exactly in terms of a truncated Fourier series, and scalar values outside the interval [0,1] appear. In order to reduce the magnitude of these values, the initial scalar profile is obtained after integrating the pure diffusion equation several times.

Several types of initialization have been examined: (1) a rectangular slab with half-width of 1 grid space slightly smoothed by integrating the pure diffusion equation once (*Run* 1); (2) a profile obtained by integrating the pure diffusion equation for the previous profile several times (*Run* 2); (3) a Gaussian profile with $A \equiv \int_{y_1=1}^{y_2=128} \overline{Y}\,\mathrm{d}y = 2$ (*Run* 3); and (4) a triangular slab with half-width of 0.5 (*Run* 4). For *Runs* 1–3, $A = 2$ and *Run* 4 has $A = 1$. The initial scalar profiles for *Runs* 1 to 4 are presented in figure 2. It can be seen that when the initial scalar profile is smooth (*Run* 2 and *Run* 3), the magnitude of the negative values of Y is very small. During the development time, when the scalar fluctuations are generated, some of the points with negative values tend to increase their magnitude. After a short time compared to the duration of the simulation, turbulent mixing becomes important and the magnitudes of the negative scalar values decrease significantly. Table 2 presents the magnitudes of the highest negative value, the numerical time t' when it was obtained, and the percentage of points with negative scalar values in the corresponding (x, z)-plane.

The highest negative values were obtained for the run which initializes the scalar field with a triangular slab, as expected, and the smallest negative values were obtained for *Run* 2. Scalar values over 1.0 also appear for *Run* 1 and for the wider initial scalar profiles discussed in § 4.2 (*Run* 5 to *Run* 8). However, these values rapidly fall below 1.0 as the scalar wake is spreading. At the same time, the numerical oscillations seen in figure 2 on the initial scalar profiles are no longer present on the mean scalar profiles (not shown) after only few iterations. Additionally, two-dimensional spectra of the scalar variance (not shown here) indicate that all the scalar scales are well resolved. Amongst the initial scalar profiles used, the Gaussian profile has a small number of points with scalar values outside [0, 1], yet maintaining a thin profile. Also, this profile is closest to the profiles obtained by experiments. The simulation which initializes the scalar field with this profile (*Run* 3), is taken as the base run in the subsequent sections.

https://doi.org/10.1017/S0022112000008910 Published online by Cambridge University Press

	Run 1	*Run* 2	*Run* 3	*Run* 4
Highest negative value	−0.12	−0.025	−0.08	−0.23
t'	0.24	0.24	0.24	0.09
Points with negative values	6%	1%	4%	25%

TABLE 2. The highest negative scalar values obtained during different runs.

x/M	52	60	100
t	5.61	6.18	9.09
t/t_{ref}	3.12	3.438	5.057
$(Re_\lambda)_{exp}$	44	43	39
$(Re_\lambda)_{DNS}$	44	42.6	36.86
$(\eta_K/L_{ref})_{exp}$	0.0261	0.0284	0.0387
$(\eta_K/L_{ref})_{DNS}$	0.0261	0.0283	0.0383
$\eta_K k_{max}$	1.275	1.385	1.87
$(L/L_{ref})_{exp}$	1.00	1.06	1.22
$(L/L_{ref})_{DNS}$	1.00	1.03	1.12
$(\tau/t_{ref})_{exp}$	1.00	1.16	1.92
$(\tau/t_{ref})_{DNS}$	1.00	1.14	1.80

TABLE 3. Velocity field parameters for W84 and DNS.

3. Velocity field

The velocity field from W84 was simulated between the location of the heated wire ($x/M = 52$) and $x/M = 100$. However, the scalar field simulation was stopped at $x/M = 90$ ($t = 8.37$), in order to prevent the wake reaching the boundaries.

Knowing the reference scales (table 1), the numerical quantities can be directly compared to the experimental ones. Numerical values for some parameters of the velocity field are listed in table 3. There is a good agreement between the W84 and DNS results.

The energy decay law for $52 < x/M < 90$ was calculated to be

$$\frac{u_{rms}^2}{U^2} = 0.149\left(\frac{x}{M}\right)^{-1.45}, \tag{3.1}$$

and has a decay exponent close to the 1.4 that was determined in W84 for the decay law of the longitudinal mean-square velocity fluctuations .

In order to test the influence of the random number generator on the results obtained, the velocity field was initialized using a different seed and a second simulation was carried out. Following the same procedure as described above, the numerical time corresponding to the location of the heated wire and the reference scales were calculated. The normalized statistics pertaining to the velocity field are almost identical for the two runs at corresponding times.

4. Scalar field

4.1. *Scalar wake generated by a thin source*

The development of the mean scalar wake corresponding to a source size smaller than the Kolmogorov microscale has three distinct stages: molecular diffusive, turbulent convective, and turbulent diffusive (e.g. Warhaft 1984; Anand & Pope 1985). The first stage is characterized by length scales smaller than the Kolmogorov microscale

https://doi.org/10.1017/S0022112000008910 Published online by Cambridge University Press

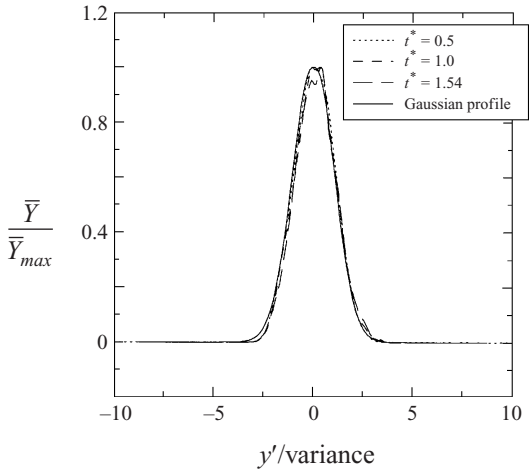


FIGURE 3. Mean scalar profiles at different times for *Run* 3; $y' = y - 64.5$.

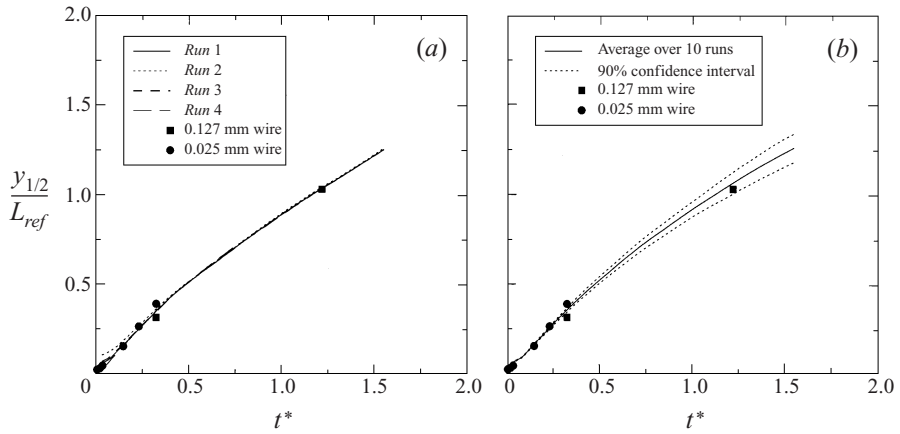


FIGURE 4. Time evolution of (*a*) half-width of the scalar wake, and (*b*) average half-width of the scalar wake.

and for the value of Re_λ considered in this work it is computationally infeasible to simulate this stage. Neither the W84 experiment nor the DNS extend far enough to capture the third stage. The second stage is entirely simulated, as well as part of the transition to the third stage. Using the reference scales one can calculate the length of the computational domain, 104 mm, and the grid spacing, 0.82 mm. Since both wires used in W84 have diameters smaller than the grid spacing, the wake cannot be simulated from the location of the heated wire, but from where it becomes larger than the grid size. Nevertheless, the simulation of the W84 scalar wake starts at a dimension of the same order of magnitude as Kolmogorov microscale. When the scalar wake is smaller than the Kolmogorov microscale, in the molecular diffusive regime, it is hardly affected by the turbulence field and has little internal structure, so its history is not important. Thus, the simulation results of the scalar field can be directly compared to W84. For all the simulations presented in this section, the scalar field is generated at $t^* = t'/(t_{ref})_{DNS} = 0.027$.

In numerical simulations the initial scalar field has no fluctuations and they are generated during a development time. After this initial development time the mean

https://doi.org/10.1017/S0022112000008910 Published online by Cambridge University Press

scalar profiles approach a Gaussian shape in agreement with the experimental data (W84; Stapountzis *et al.* 1986; Li & Bilger 1996). Figure 3 compares the mean scalar profiles with the Gaussian curve for *Run* 3 at different times. The profiles obtained for the other runs (not shown here) collapse well after the development time. The integral $A = \int_{y_1=1}^{y_2=128} \overline{Y}\,\mathrm{d}y$ is conserved for all the simulations. The time evolution of the half-width of the mean scalar profiles, $y_{1/2}$, is presented in figure 4(*a*). There is a good agreement between the W84 and DNS results. The turbulent convective regime extends to $x'/M = 8.1$ (or $t^* = 0.33$) which is the location where the measurements started to be taken for the thicker wire. At this location, according to W84, the mean scalar half-width measurements corresponding to the thin and thick wire should match. In the turbulent convective region, the linear relation determined experimentally:

$$\frac{y_{1/2}}{L_{ref}} = 1.18\frac{u_{2_{rms}}}{u_{1_{rms}}}\frac{t}{t_{ref}}, \tag{4.1}$$

also holds for the numerical points. The initial development region is longest for *Run* 2 which starts with the largest half-width of the scalar profile and shortest for *Run* 4 which starts with the thinnest half-width of the scalar profile. *Runs* 1, 3 and 4 have basically the same half-width for the mean scalar wake after the development region.

The influence of the random number generator seed on the development of the scalar wake is assessed by using a second velocity field generated with the same parameters but a different seed (see § 3). It should be pointed out that, since the reference scales are different for the two simulations, the initial width of the scalar slab is different. In order to make a meaningful comparison, the profile used for initializing the scalar field in *Run* 1 was considered, as it gave a smaller difference in the actual size of the initial scalar field. For each velocity field, five scalar fields with the same initial profile, but at different y-locations were considered, resulting in a total of 10 runs. Different statistics of the scalar wake were calculated and compared at corresponding times. Averages and confidence intervals based on these statistics were determined. Figure 4(*b*) presents the average over the 10 runs of the normalized half-width of the mean scalar wake. The 90% confidence interval was calculated using the Student-t distribution with nine degrees of freedom. Throughout the turbulent convective regime the results are very close for all the runs. As expected, towards the end of the simulation the dispersion in the results increases among the 10 runs, but the agreement with the experimental data remains fairly good.

The r.m.s. scalar profiles (not shown here) are initially double peaked, in agreement with the experiment. After the development time they become single peaked, but the DNS do not extend far enough to verify the re-emergence of the double peak observed in W84 far downstream. The time evolution of the half-width of the r.m.s. scalar wake, $y_{rms_{1/2}}$, is presented in figure 5(*a*). Since the scalar fluctuations are generated first at the edges of the scalar wake, the initial values of $y_{rms_{1/2}}$ depend on the details of the scalar source. After an initial development time, the results obtained for runs 1, 3 and 4 are almost identical and in good agreement with the W84 data. Again, *Run* 2 has a longer development time, but $y_{rms_{1/2}}$ for this run approaches the results for the other runs later in time. The half-width of the scalar r.m.s. wake was also determined for the 10 runs described above. The time evolution of the average of $y_{rms_{1/2}}$ for the 10 runs and its 90% confidence interval are presented in figure 5(*b*). The results agree with the experimental data, although they are slightly underpredicted. The dispersion in the results obtained for the 10 runs remains small even at the end of the simulation.

https://doi.org/10.1017/S0022112000008910 Published online by Cambridge University Press

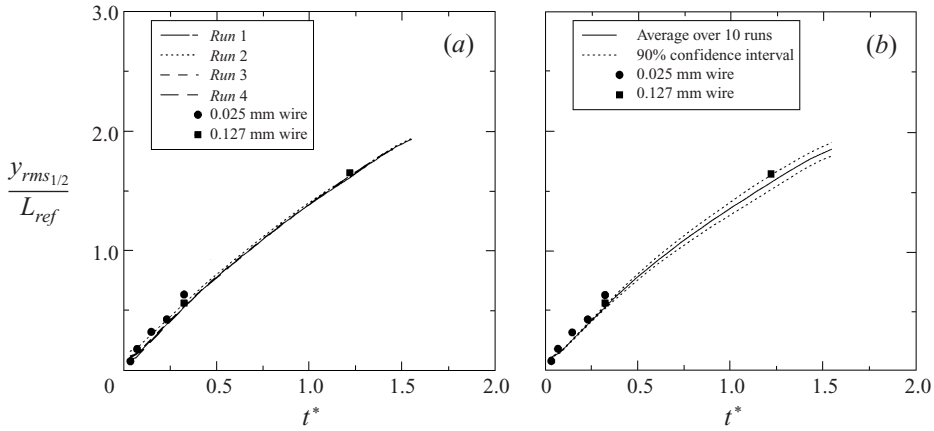


FIGURE 5. Time variation of (*a*) half-width of the scalar r.m.s. wake, and (*b*) averaged half-width of the scalar r.m.s. wake.

The ratio $s = Y_{rms}/\overline{Y}$ (scalar intensity) at the centreline is shown in figure 6. Since for our computational grid there is an even number of y-planes, all the statistics at the centreline are calculated as the average of the statistics in the two central y-planes (numbered 64 and 65). In W84, s asymptotically approaches a constant value of 0.7. This is different from the results of Stapountzis *et al.* (1986) in which the asymptotic value was 0.5 and the results of Li & Bilger (1996) which suggested that the asymptotic value should be less than 0.3. Although the numerical simulations cannot be extended to show the far-field behaviour, the results are in good agreement with the W84 data for the time range simulated. At the initiation of the scalar field $s = 0$, since there are no scalar fluctuations, and it increases as these fluctuations are produced in the field. The scalar fluctuations are generated initially at the edges of the scalar wake by the presence of the non-zero mean scalar gradient. *Run* 2 has the widest initial scalar profile and, as a result, the smallest mean scalar gradients. Consequently, the scalar fluctuations are generated at a lower rate and s increases with the smallest slope. On the other hand, *Run* 4 has the sharpest initial scalar profile and the largest mean scalar gradients, which results in the highest growth rate for s. After reaching a maximum value, s decreases due to the spreading of the wake. Consequently, the values of s for all runs have a peak which decreases in magnitude as the initial half-width of the profile increases. At the final stages of the simulations the value of s is still decreasing and it is smaller for *Run* 2 than for the other simulations. This suggests that the shape of the initial scalar profile could have long lasting influence on the values of s.

After discussing the evolution of the global scalar quantities, the structure of the scalar wake is examined in order to identify different mechanisms responsible for the spreading of the wake. Figure 7 shows the scalar PDFs at the centreline for *Run* 3. At early times the wake has little internal structure and the scalar is almost uniform at the centreline, as shown by the PDF at $t^* = 0.03$. Later in time, the wake starts meandering and the double peak in the PDF at $t^* = 0.15$ suggests that at the centreline there are regions of high and low scalar values with relatively little mixing. An instantaneous view of the scalar wake (figure 8*a*) clearly shows that the scalar wake is mainly flapping around the centreline, maintaining its compactness. At $t^* = 0.23$ the PDF is again single peaked, with the peak at very small values of the scalar. This indicates that at the centreline there are mostly regions with low scalar

https://doi.org/10.1017/S0022112000008910 Published online by Cambridge University Press

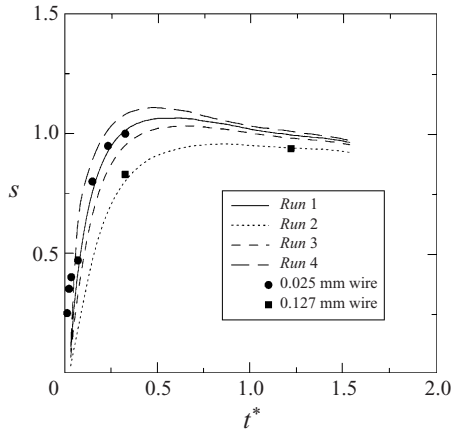


FIGURE 6. Scalar intensity on the centreline vs. time.

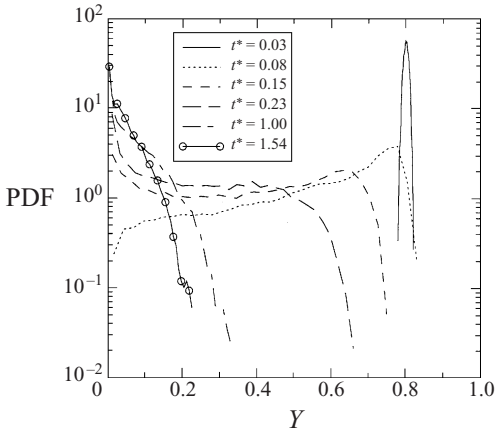


FIGURE 7. Scalar PDF at the centreline for *Run* 3.

mass fractions. The peak in the PDF at high scalar values observed at $t^* = 0.15$ is replaced now by a plateau, indicating that regions of intermediate and high scalar mass fractions are still present at the centreline. Although the wake has more internal structure, these regions retain the consistency of the wake and the flapping around the centreline can still be observed in figure 8(*b*). At later times the shape of the PDF of Y indicates that the high and low scalar mass fraction values are not well separated. This suggests that the mixing at the centreline has become significant. At this stage, the wake is much wider compared to its initial size and has a complex internal structure (figure 8*c*). Also, the flapping around the centreline can no longer be seen. These results agree qualitatively with the experimental results obtained by Stapountzis *et al.* (1986).

In order to quantify the contribution of the flapping around the centreline to the structure of the wake we follow the approach proposed by Anand & Pope (1985). The scalar variance ($\overline{Y'^2}(y,t)$) is written as the sum of the contribution from internal structure of the wake ($\overline{Y_c'^2}$) and the contribution from the flapping around the centreline ($\overline{Y_{flap}'^2}$). This decomposition is possible from the observation that, at very early times, the scalar wake behaves like a laminar wake convected laterally by the

https://doi.org/10.1017/S0022112000008910 Published online by Cambridge University Press

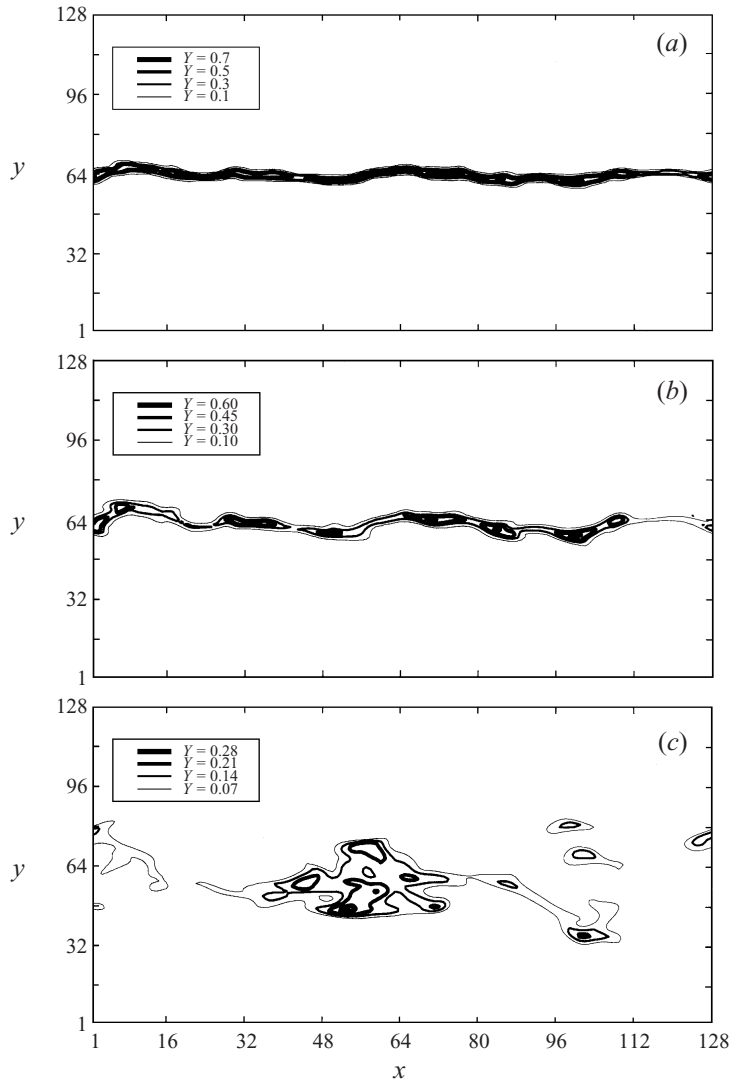


FIGURE 8. Instantaneous scalar wake for *Run* 3. Scalar profiles obtained at $z = 64$ and (*a*) $t^* = 0.15$, (*b*) $t^* = 0.23$, (*c*) $t^* = 1.0$. The coordinates x, y and z represent the grid points in the x-, y- and z-directions, respectively.

y-component of the velocity, v. The most important random variable for the wake development at early times is, then, the velocity v at the location of the scalar source. Consequently, the statistical quantities are calculated by conditioning on $v_0 = \hat{v}$, where

$$v_0 = v(y' = 0, t' = 0), \tag{4.2}$$

$\hat{v}$ is the sample space variable for v and $y' = y - 64.5$. By using the conditional mean ($\tilde{Y} \equiv \overline{Y|\hat{v}}$), the scalar fluctuations can be decomposed into two parts:

$$Y' = (\tilde{Y} - \overline{Y}) + Y'', \tag{4.3}$$

where $Y'' \equiv Y - \tilde{Y}$ denotes the fluctuations about the conditional mean. The scalar

https://doi.org/10.1017/S0022112000008910 Published online by Cambridge University Press

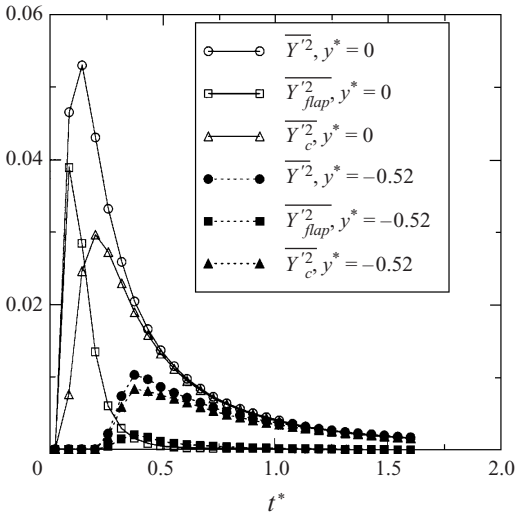


FIGURE 9. Time evolution of $\overline{Y'^2}$, $\overline{Y'^2_{flap}}$ and $\overline{Y'^2_c}$ at $y^* = 0$ and $y^* = -0.52$ for *Run* 3.

variance can then be expressed as

$$\overline{Y'^2} = \underbrace{\int_{-\infty}^{\infty} g(\hat{v})(\tilde{Y} - \overline{Y})^2 \mathrm{d}\hat{v}}_{\overline{Y'^2_{flap}}} + \underbrace{\int_{-\infty}^{\infty} g(\hat{v})\widetilde{Y''^2}\mathrm{d}\hat{v}}_{\overline{Y'^2_c}}, \tag{4.4}$$

where $g(\hat{v})$ is the PDF of v at $y' = 0, t' = 0$ and the conditional variance is $\widetilde{Y''^2} \equiv \overline{Y''^2|\hat{v}}$. For the numerical calculations, v_0 was taken as the velocity v at $t^* = 0.027$, corresponding to the time when the scalar field is initialized, and $y^* = y'/L_{ref} = 0$. Figure 9 shows the time evolution of the scalar variance and its components at $y^* = 0$ and $y^* = -0.52$. For our computational domain, $-3.86 < y^* < 3.86$; $y^* = -0.52$ corresponds to y-plane number 56. Initially, the scalar variance and its components are zero, since the scalar field has no fluctuations. As the scalar fluctuations are generated in the field the scalar variance increases. After reaching a maximum, $\overline{Y'^2}$ starts to decrease, as the wake spreads. At the centreline, most of the contribution to the scalar variance is from the flapping component at early times. As the wake develops, this contribution decreases and becomes negligible after the end of the turbulent convective regime ($t^* > 0.33$). Away from the centreline, the time delay after which the scalar variance starts to increase corresponds to the time it takes the scalar wake to reach the observation point. Since the wake has already developed internal structure by the time it reaches $y^* = -0.52$, the contribution from the component associated with the internal structure is dominant at all times at this location.

It is interesting now to compare the profiles of $\overline{Y'^2}$, $\overline{Y'^2_{flap}}$ and $\overline{Y'^2_c}$ across the wake, at different times (figure 10). As mentioned before, the scalar variance profile is double peaked at early times, then it becomes single peaked. The profile of $\overline{Y'^2_c}$ is single peaked at all times, unlike the profile of the flapping component which is double peaked at early times ($t^* < 0.33$). Initially (not shown here) the flapping component is dominant at all locations across the wake and becomes less significant at later times. At $t^* = 0.15$ (figure 10*a*) the two components are equally important

https://doi.org/10.1017/S0022112000008910 Published online by Cambridge University Press

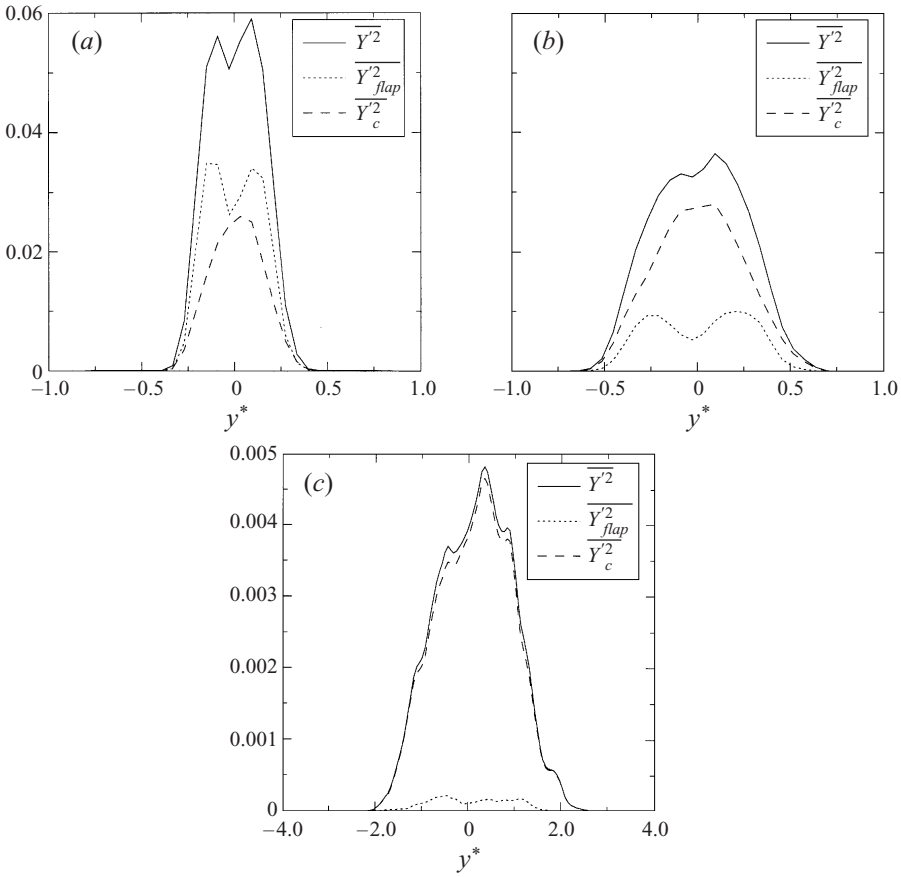


FIGURE 10. Profiles of $\overline{Y'^2}$, $\overline{Y'^2_{flap}}$ and $\overline{Y'^2_c}$ for *Run* 3 at (*a*) $t^* = 0.15$, (*b*) $t^* = 0.23$, (*c*) $t^* = 1.0$.

across the wake. Later, as shown in figure 10(*b*), $\overline{Y'^2_c}$ becomes more important at all y-locations across the wake. The relative magnitude of $\overline{Y'^2_{flap}}$ decreases continuously compared to $\overline{Y'^2_c}$ in this stage and it becomes negligible in the transition regime toward the turbulent diffusive regime (figure 10*c*).

In order to obtain the global contributions of the flapping around the centreline and internal structure to the scalar variance, the profiles of the scalar variance and its components are integrated across the wake:

$$I \equiv \int_{y_1=1}^{y_2=128} \overline{Y'^2} \mathrm{d}y, \tag{4.5}$$

$$I_{flap} \equiv \int_{y_1=1}^{y_2=128} \overline{Y'^2_{flap}} \mathrm{d}y, \tag{4.6}$$

$$I_c \equiv \int_{y_1=1}^{y_2=128} \overline{Y'^2_c} \mathrm{d}y. \tag{4.7}$$

Figure 11 shows the time evolution of I, I_{flap} and I_c for *Run* 3 and W84. In order to make a meaningful comparison between the DNS and the experimental results, the scalar field is normalized by the area under the scalar mean profiles, A. Since in the

https://doi.org/10.1017/S0022112000008910 Published online by Cambridge University Press

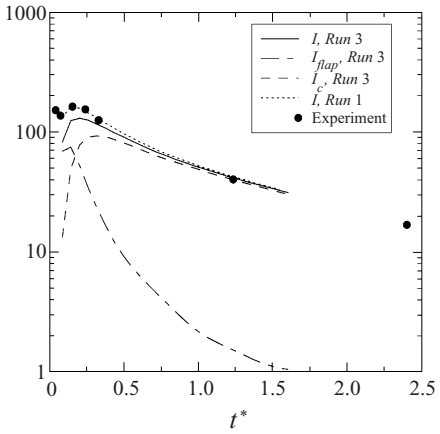


FIGURE 11. Time variation of scaled I, I_{flap} and I_c.

numerical simulation the scalar field is initialized later than in the actual experiment, there is a difference between the experimental and numerical values of I at early times. Nonetheless, after the development time the results agree well. As mentioned before, the development time depends on the details of the scalar source, in particular on the initial mean scalar gradients. For comparison we also plotted in figure 11 the time variation of I for *Run* 1, which is initialized with a sharper scalar profile. In this case, the numerical results agree with the experimental points even at early times. The total contribution across the wake of the flapping component to the scalar variance is large at early times, as expected, and is very small at later times. It appears that, after the end of the turbulent convective regime, the contribution of the internal structure to the scalar variance becomes dominant.

In addition to the scalar variance, higher moments of the scalar PDF have also been examined experimentally. Figure 12 shows the kurtosis versus skewness of the scalar for *Run* 3 and the best curve fits through the data of Mole & Jones (1994) and Li & Bilger (1996). The numerical data suggest the existence of a simple relationship between K and S. In general the data seem to follow the relation $K = aS^2 + b$, as proposed by Mole & Clarke (1995). In order to test the influence of the Reynolds number on the results, several simulations were carried out at lower Re_0 (see § 2.3) and the scalar initialization used for *Run* 3. The results change slightly with the Reynolds number, but no clear trend has been observed for the range of Reynolds numbers studied.

4.2. *Influence of the source size on the development of the scalar wake*

In this section the effects of source size on the development of the scalar wake are studied. The scalar source has diameters ranging from the Kolmogorov microscale to the integral scale of the turbulence. The large source sizes are difficult to study experimentally due to the influence of the wire on the velocity field and the vortex shedding from the wire. Table 4 shows the half-width of the initial scalar slabs for runs 5–8, and their relative size compared to the η_K and the integral scale. The initial scalar profiles for runs 5–8 are obtained following the same procedure as for *Run* 1, but using wider 'rectangular' scalar slabs. For all these runs the velocity field is generated using the same initial conditions as before and the scalar transport equation is integrated from $t' = 0$.

https://doi.org/10.1017/S0022112000008910 Published online by Cambridge University Press

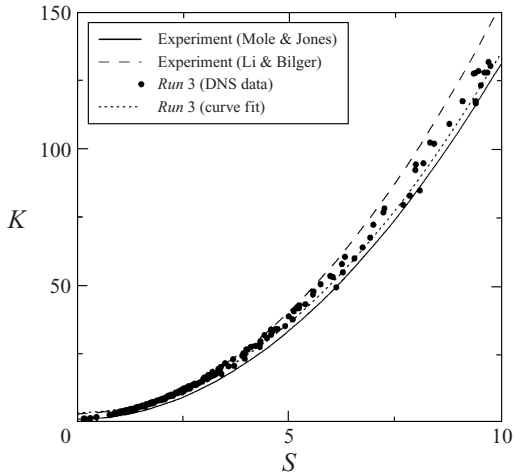


FIGURE 12. Kurtosis vs. skewness of the scalar mass fraction across the wake and in time; $K = 1.33S^2 + 3.18$ (*Run* 3), $K = 1.5S^2 + 2.8$ (Li & Bilger), $K = 1.31S^2 + 0.77$ (Mole & Jones). The sample size for curve fitting was 1200 points.

	Run 5	*Run* 6	*Run* 7	*Run* 8
$y_{1/2}$[grid space]	1	2	4	8
$y_{1/2}/\eta_K$	2.33	4.65	9.31	18.61
$y_{1/2}/L$	0.06	0.12	0.24	0.49

TABLE 4. Initial scalar slab width.

Figure 13(*a*) presents the variation of the half-width of the mean scalar wake for all the source sizes analysed. After the initial development time when the scalar fluctuations develop in the field, the rate of growth of the half-width of the mean scalar wake becomes independent of the source size. Also, after the development time, the mean scalar profiles (not shown here) approach a Gaussian shape. The half-width of the r.m.s. scalar wake (figure 13*b*) exhibits a behaviour similar to that of the half-width of the mean scalar wake. After an initial development time (whose duration is shorter for the r.m.s. wake) the rate of growth becomes approximatively independent of the source size. Analysis of the scalar intensity at the centreline for different source sizes (not shown here) indicates a strong dependence on the source size for the time range simulated. Similarly to the evolution of s presented in figure 6, for larger source sizes s has a peak which decreases in magnitude and occurs at later times as the source size increases. This behaviour can be explained by noticing that the scalar fluctuations at the centreline are generated earlier for the thinner source sizes. As a result, they will reach the maximum intensity sooner.

As the initial source size increases, the structure of the scalar wake also changes. For the largest source size simulated (*Run* 8), the scalar PDF at the centreline (figure 14) remains single peaked for a longer time than the thin source size results shown in figure 7. At initial times the scalar wake, which in this case is larger than most of the turbulent eddies, is primarily affected by the turbulent motion at the edges and only slightly convected laterally (figure 15*a*, *b*). Consequently, at the centreline there

https://doi.org/10.1017/S0022112000008910 Published online by Cambridge University Press

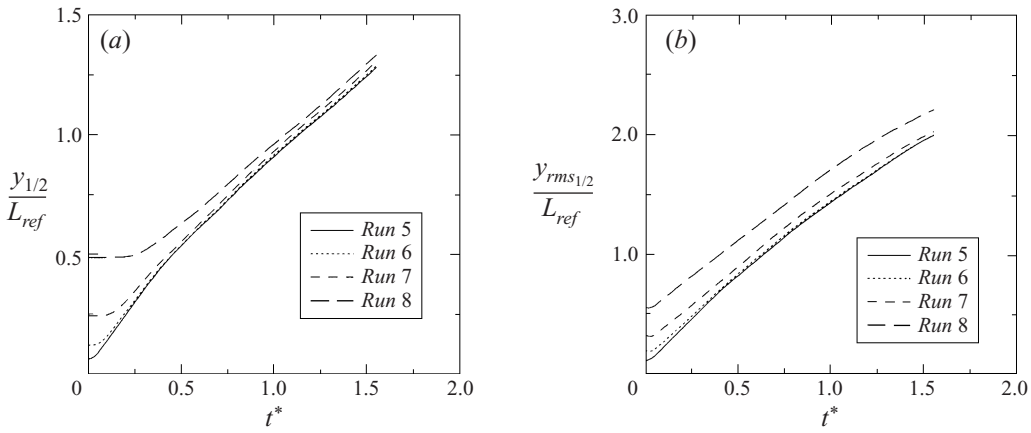


FIGURE 13. (*a*) Time evolution of the half-width of the scalar wake for different source sizes. (*b*) Half-width of the r.m.s. scalar wake vs. time for different source sizes.

are mainly regions with high scalar values even at $t^* = 0.23$. The effect of the large eddies begins to be visible later when, as figure 15(*c*) shows, the wake starts to lose its compactness. At $t^* = 0.5$ (figure 14) the scalar PDF at the centreline is double peaked with the peaks at very large and very small scalar values. This indicates that at the centreline there are mainly patches of low and high scalar mass fractions. But, unlike the smaller source sizes where the double peak in the scalar PDF was associated with the compact wake flapping around the centreline, in this case the flapping mechanism is no longer responsible for the appearance of the double peak. Towards the end of the simulation the scalar PDF becomes single peaked again, with the peak at small scalar values. But, as the scalar PDF shows, even at the end of the simulation ($t^* = 1.5$), there are still regions on the centreline with high scalar mass fractions corresponding to little mixing. In order to analyse quantitatively the influence of the source size on the structure of the scalar wake, the methodology described in § 4.1 can be extended and the contributions due to flapping and internal structure of the wake to the scalar variance can be found. All scalar variance profiles obtained (not shown here) are double peaked at early times and, as expected, $\overline{Y_{flap}'^2}$ is small compared to $\overline{Y_c'^2}$ at all times.

4.3. *Turbulent transport of the scalar field* (*DNS and models*)

The scalar field is homogeneous in the x- and z-directions and inhomogeneous in the y-direction. Using the governing equations presented in § 2.2, the transport equations for different scalar moments can be derived. The relative importance of various terms in these equations can identify the mechanisms of mixing and transport of the scalar field by the turbulence.

Figures 16, 17, 21 and 22, presenting the terms in the transport equations discussed in this section, were obtained from *Run* 3. All the other runs provide similar results. In these figures, RHS refers to the sum of the terms on the right-hand side of the equation, and LHS is the time derivative which is calculated separately. As expected, the right- and left-hand sides of the transport equations presented in figures 16, 17, 21 and 22 are in good agreement. All the temporal evolutions presented in this section

https://doi.org/10.1017/S0022112000008910 Published online by Cambridge University Press

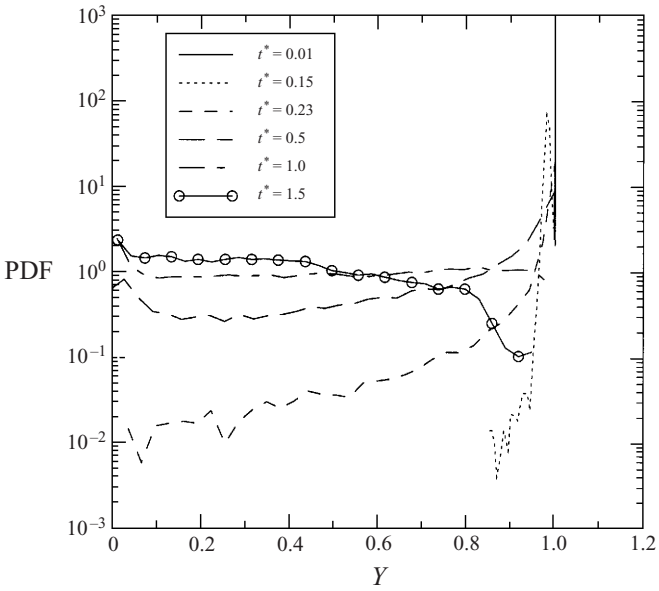


FIGURE 14. Scalar PDF at the centreline for *Run* 8.

start at $t^* = 0.15$, corresponding to the location of an W84 experimental point, which is after the initial development time.

4.3.1. *Mean scalar and scalar flux*

The equation for the mean scalar is

$$\frac{\partial \overline{Y}}{\partial t} = \underbrace{-\frac{\partial}{\partial y}(\overline{vY'})}_{\text{I}} \underbrace{+\frac{1}{Re_0 Sc}\frac{\partial^2 \overline{Y}}{\partial y^2}}_{\text{II}}, \tag{4.8}$$

where $v = u_2$ and the averages are taken over the homogeneous directions for each y-plane.

The first term on the right-hand side of equation (4.8) is the turbulent transport of the scalar fluctuations, which contributes most to the RHS, and the second term is molecular diffusion of the mean scalar field. At the centreline (not shown), the RHS has negative values at all times indicating a continuous decay of the mean scalar after the development time. However, at $y^* = -0.52$ (figure 16*a*), the scalar mass fraction is zero at $t^* = 0.15$, and the mean scalar values increase as the wake approaches this location. The time variation of the terms in equation (4.8) at $y^* = -0.52$ shows that the RHS increases from zero at $t^* = 0.15$ to a peak value then becomes negative at later times. The magnitude of the negative values of the RHS are much smaller than its peak value. This indicates that the mean scalar, after reaching a peak value, decreases slowly as the wake is spreading.

It is also interesting to examine the terms in the mean scalar equation across the wake. Figure 16(*b*) presents the y variation of the terms in equation (4.8) at $t^* = 0.23$, corresponding to an W84 experimental point in the turbulent convective regime. The diffusion term is small compared to the first term throughout the width of the wake, as expected in the turbulent convective regime. The turbu-

https://doi.org/10.1017/S0022112000008910 Published online by Cambridge University Press

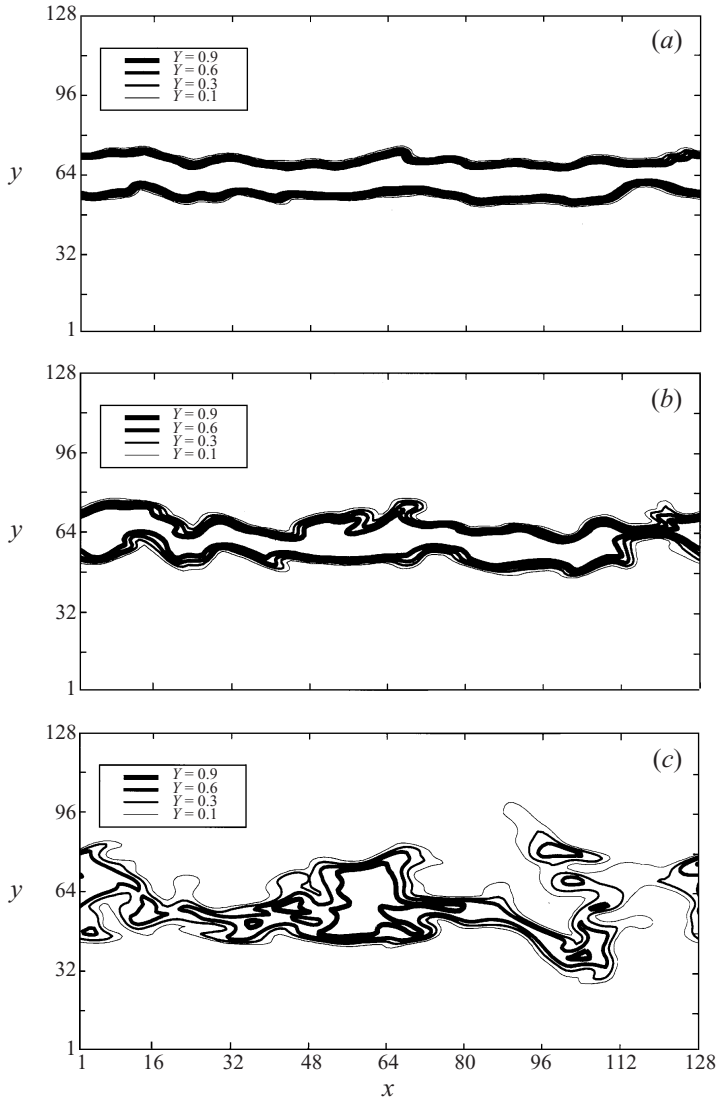


FIGURE 15. Instantaneous scalar wake for *Run* 8. Scalar profiles obtained at $z = 64$ and (*a*) $t^* = 0.15$, (*b*) $t^* = 0.23$, (*c*) $t^* = 1.0$. The coordinates x, y and z represent the grid points in the x-, y- and z-directions, respectively.

lent transport term is symmetric with respect to the centreline, with positive values near the outer edges of the wake, and negative values in the central region. The scalar fluctuations are thus transported from the inner regions of the wake toward the outer edges. This is the main mechanism responsible for the spreading of the mean scalar wake. At later times, as the wake develops, the terms in equation (4.8) fluctuate more across it, but all the features explained above are preserved (figure 16*c*).

The most important quantity on the right-hand side of the mean scalar equation is the derivative of the scalar flux. The scalar flux is also part of the production term in the scalar variance equation, (4.17) below. The transport equation for the scalar flux

https://doi.org/10.1017/S0022112000008910 Published online by Cambridge University Press

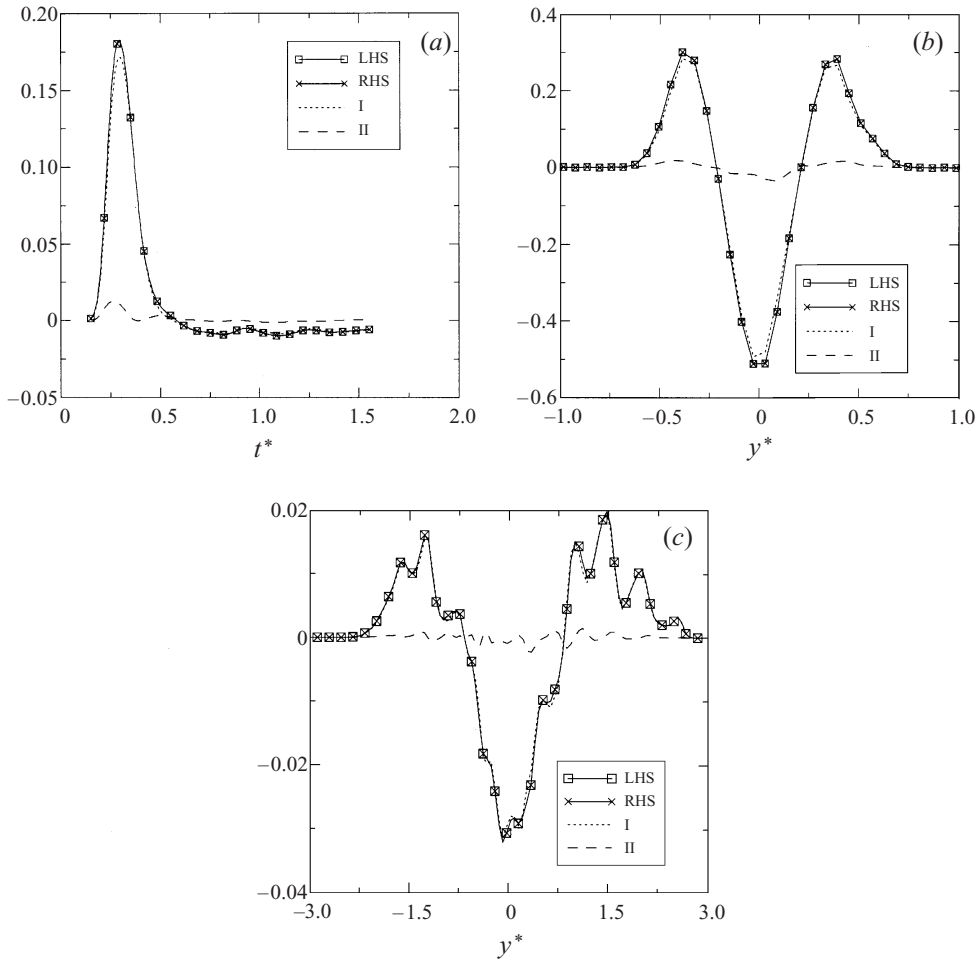


FIGURE 16. (*a*) Time variation of the terms in mean scalar equation (4.8) for *Run* 3 at $y^* = -0.52$; the terms in the mean scalar equation across the wake at (*b*) $t^* = 0.23$, (*c*) $t^* = 1.0$.

in the y-direction can be written as

$$\frac{\partial(\overline{vY'})}{\partial t} = \underbrace{-\frac{\partial}{\partial y}(\overline{v^2Y'})}_{\mathrm{I}} \underbrace{-\overline{v^2}\frac{\partial \overline{Y}}{\partial y}}_{\mathrm{II}} \underbrace{-\frac{1}{\rho_0}\left(\overline{Y'\frac{\partial p}{\partial y}}\right)}_{\mathrm{III}} \underbrace{+\frac{\partial}{\partial y}\left[\frac{1}{Re_0 Sc}\left(\overline{v\frac{\partial Y'}{\partial y}}\right)+\frac{1}{Re_0}\left(\overline{Y'\frac{\partial v}{\partial y}}\right)\right]}_{\mathrm{IV}}$$
$$\underbrace{-\left(\frac{1}{Re_0 Sc}+\frac{1}{Re_0}\right)\left(\overline{\frac{\partial Y'}{\partial x_j}\frac{\partial v}{\partial x_j}}\right)}_{\mathrm{V}}. \qquad (4.9)$$

The terms on the right-hand side of equation (4.9) are (I) turbulent diffusion, (II) production due to the mean scalar gradient, (III) pressure scrambling, (IV) molecular diffusion and (V) dissipation, respectively. Due to the symmetry of the problem, the turbulent scalar flux should be statistically zero on the centreline, with positive values for $y^* > 0$ and negative for $y^* < 0$. Figure 17(*a*) presents the time variation of the terms in equation (4.9) at $y^* = -0.52$. As the wake reaches this point, the magnitude of $\overline{vY'}$ increases (becomes more negative) as shown by the variation of the

https://doi.org/10.1017/S0022112000008910 Published online by Cambridge University Press

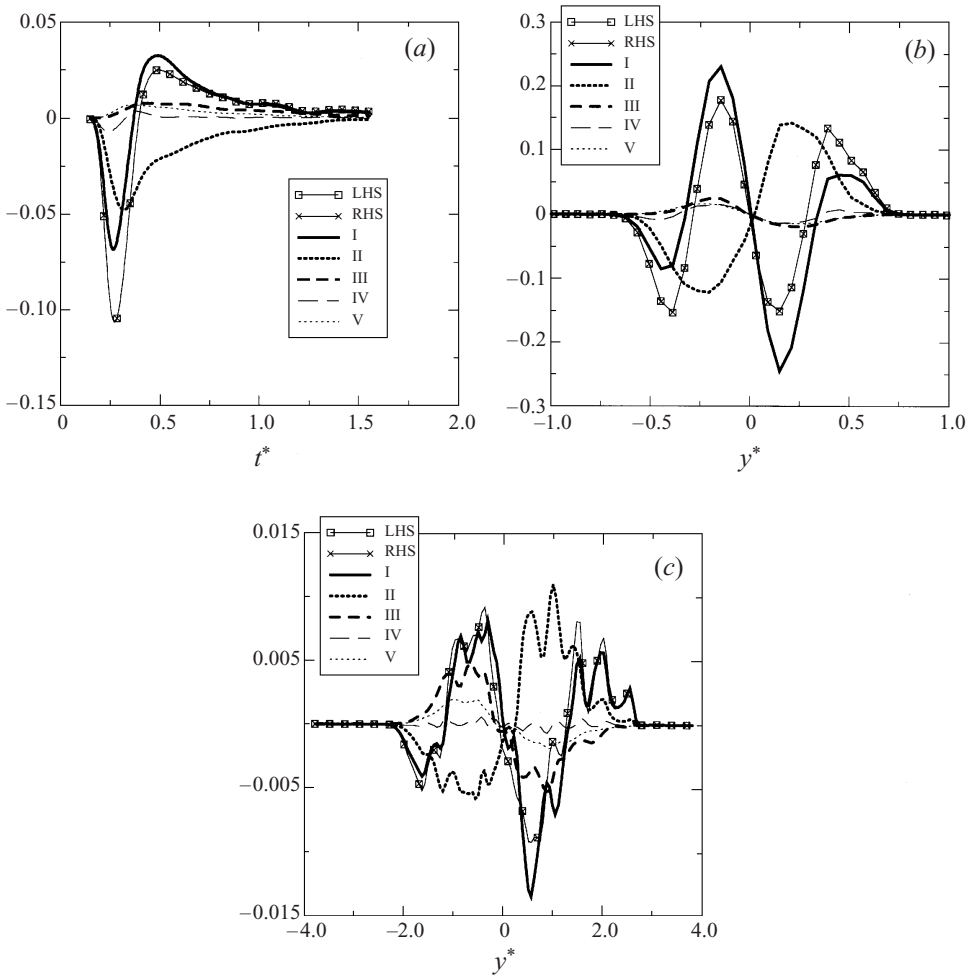


FIGURE 17. (*a*) Time evolution of the terms in scalar flux equation (4.9) for *Run* 3 at $y^* = -0.52$; the terms in the scalar flux equation across the wake at (*b*) $t^* = 0.23$, (*c*) $t^* = 1.0$.

RHS. However, for $t^* > 0.4$ the time derivative of the scalar flux becomes positive, indicating that, after reaching a peak, the scalar flux starts to decay. The turbulent transport term follows the variation of the RHS, being the most important term at all times. The production term consists of the product of the mean scalar gradient and the variance of the velocity v. After reaching a peak value, this term decreases as the turbulent energy decays and as the mean scalar wake spreads. Figure 17(*a*) also shows that terms III, IV and V are small during the simulation. As the wake reaches $y^* = -0.52$, the magnitude of the turbulent scalar flux is increased primarily by turbulent transport term and the production term (I and II). At later times, when the scalar flux starts to decay, term I is almost equal to the RHS, while the production term is balanced by the sum of the pressure-scrambling and dissipation terms (III and V).

In order to gain a better understanding of how the scalar flux is generated and transported across the wake, the y-variation of the terms in equation (4.9) is examined in figure 17(*b*) at $t^* = 0.23$. All the terms are antisymmetric with respect to the

https://doi.org/10.1017/S0022112000008910 Published online by Cambridge University Press

centreline, consistent with the variation of the scalar flux across the wake. At $t^* = 0.23$, the pressure-scrambling and the molecular terms are small at all y-locations, so the RHS is given by the balance between the turbulent transport and the production terms. The y-dependence of the production term is due to the mean scalar gradient, and it follows the shape of the derivative of a Gaussian curve. It reaches a maximum value at a certain y-location and decreases to zero at the centreline. The sign of the turbulent diffusion term is opposite to that of the production term (acts as a destruction term) for $-0.35 < y^* < 0.35$, and redistributes the scalar flux toward the outer regions of the wake. For $|y^*| > 0.35$ terms I and II have the same sign, and both contribute to the increase of the scalar flux magnitude. Near the outer edges of the wake, the turbulent diffusion term is dominant. This indicates that term I is primarily responsible for the increase in the scalar flux in these regions. At later times (figure 17*c*), the pressure-scrambling term becomes comparable with I and II and acts as a destruction term at all y-locations.

The scalar flux term in the mean scalar equation (4.8) is usually closed by using a gradient diffusion model (Anand & Pope 1985; Fox 1995):

$$\overline{vY'} = -\Gamma_t \frac{\partial \overline{Y}}{\partial y}. \tag{4.10}$$

These models have been developed for the turbulent diffusive regime and it is known that they do not work well during the early stages of the wake development (e.g. Anand & Pope 1985). Scatter plots of $\overline{vY'}$ and $\partial\overline{Y}/\partial y$ across the scalar wake at early times (not shown here) indicate a relatively weak correlation between the two quantities. But as the mean scalar profile approaches a Gaussian shape the scalar flux and the mean scalar gradient across the wake become highly correlated. In order to quantify this, the correlation coefficient between two quantities a and b is defined as

$$\zeta(a,b) \equiv \frac{\langle ab\rangle - \langle a\rangle\langle b\rangle}{[(\langle a^2\rangle - \langle a\rangle\langle a\rangle)(\langle b^2\rangle - \langle b\rangle\langle b\rangle)]^{1/2}} \tag{4.11}$$

where the averages, denoted by $\langle\ \rangle$, are taken over the y-direction (across the wake) and in time. At early times, $\zeta(\overline{vY'}, \partial\overline{Y}/\partial y) = -0.45$ and it becomes equal to -0.95 after the end of the turbulent convective regime ($t^* > 0.33$). This correlation remains high even when the source size is comparable with the integral scale ($\zeta(\overline{vY'}, \partial\overline{Y}/\partial y) = -0.97$ for *Run* 8 and $t^* > 0.33$). It should be also noted that, when calculating Γ_t from equation (4.10), a singularity occurs whenever the mean scalar gradient is very small (near the centreline and at the edges of the wake). In order to avoid this, an averaged Γ_t, Γ_{tav}, has been defined across the wake by integrating the absolute values of the scalar flux and mean scalar gradient over the y-direction and calculating their ratio at each time step. The absolute values are needed since the mean scalar gradient and the scalar flux have opposite signs for $y > 0$ and $y < 0$. Figure 18 presents the time evolution of Γ_{tav} obtained for different source sizes. For comparison, the diffusion coefficient obtained from the k–ϵ model, $\Gamma_t' \equiv (C_\mu/\sigma_f)(k^2/\epsilon)$ (Launder & Spalding 1972) is also plotted in figure 18. The model constants are $C_\mu = 0.09$ and $\sigma_f = 0.7$. The turbulent kinetic energy, k, and velocity dissipation, ϵ, are the same for the runs presented. Unlike Γ_{tav}, Γ_t' decreases continuously during the simulation. Although there is a good correlation between the scalar flux and the mean scalar gradient, the k–ϵ model does not capture well the behaviour of Γ_{tav} for the time range simulated.

The model assumption given by equation (4.10) can be relaxed by using the velocity–scalar joint PDF equation (Anand & Pope 1985). If $f(\boldsymbol{V}, \Psi; \boldsymbol{x}, t)$ is the probability density of the joint events $\boldsymbol{U}(\boldsymbol{x}, t) = \boldsymbol{V}$ and $Y(\boldsymbol{x}, t) = \Psi$, then an exact equation for f

https://doi.org/10.1017/S0022112000008910 Published online by Cambridge University Press

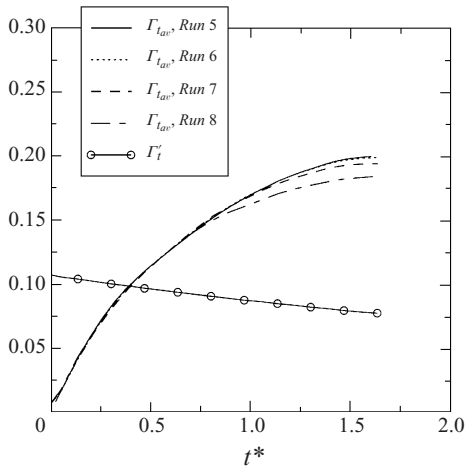


FIGURE 18. Time variation of Γ_{tav} and Γ_t' for different source sizes.

for the flow under consideration is (Pope 1985)

$$\frac{\partial f}{\partial t} + V_2 \frac{\partial f}{\partial y} = -\frac{\partial}{\partial \Psi}\left(f\left(\overline{\frac{1}{Re_0 Sc}\nabla^2 Y \,|\, \boldsymbol{V}, \Psi}\right)\right) - \frac{\partial}{\partial V_i}(f(\overline{a_i|\boldsymbol{V}, \Psi})), \tag{4.12}$$

where: $\overline{Q|\boldsymbol{V}, \Psi}$ is the expectation of the function Q upon the joint events $\boldsymbol{U} = \boldsymbol{V}$ and $Y = \Psi$, and a_i is the force per unit mass on a fluid particle:

$$a_i = \nu \frac{\partial^2 U_i}{\partial x_j \partial x_j} - \frac{1}{\rho}\frac{\partial p}{\partial x_i}. \tag{4.13}$$

By integrating equation (4.12), and using stochastic models for the terms $\nabla^2 Y$ and a_i (Pope 1985), a modelled scalar flux equation is obtained:

$$\frac{\partial(\overline{vY'})}{\partial t} + \frac{\partial(\overline{v^2 Y'})}{\partial y} + \overline{v^2}\frac{\partial(\overline{Y})}{\partial y} - \frac{1}{Re_0 Sc}\frac{\partial^2(\overline{vY'})}{\partial y^2} = -C_m \frac{\epsilon}{k}(\overline{vY'}). \tag{4.14}$$

By comparing equations (4.14) and (4.9), an expression for C_m can be derived:

$$C_m = \frac{k}{\epsilon}\frac{\overline{T}}{\overline{vY'}}, \tag{4.15}$$

where

$$\overline{T} = \frac{1}{\rho_0}\left(\overline{Y'\frac{\partial p}{\partial y}}\right) - \frac{\partial}{\partial y}\left[\frac{1}{Re_0 Sc}\left(\overline{v\frac{\partial Y'}{\partial y}}\right) + \frac{1}{Re_0}\left(\overline{Y'\frac{\partial v}{\partial y}}\right)\right] + \left(\frac{1}{Re_0 Sc} + \frac{1}{Re_0}\right)\left(\overline{\frac{\partial Y'}{\partial x_j}\frac{\partial v}{\partial x_j}}\right) + \frac{1}{Re_0 Sc}\frac{\partial^2(\overline{vY'})}{\partial y^2}. \tag{4.16}$$

After the initial development time, the scatter plots of $\overline{T}$ vs. $\overline{vY'}\epsilon/k$ in figure 19 indicate a good correlation between the two quantities across the wake for *Run* 3 ($\zeta(\overline{T}, \overline{vY'}\epsilon/k) = 0.98$). The results for all the other runs are similar. However, $\overline{T}$ and $\overline{vY'}\epsilon/k$ become less correlated as the value of Re_0 decreases (not shown). Figure 20(*a*) shows the time evolution for C_m at $y^* = -0.52$, for different initial source sizes. During the development of the scalar fluctuations, C_m has large magnitudes due to the singularity in relation (4.15). But curiously enough, following the turbulent convective

https://doi.org/10.1017/S0022112000008910 Published online by Cambridge University Press

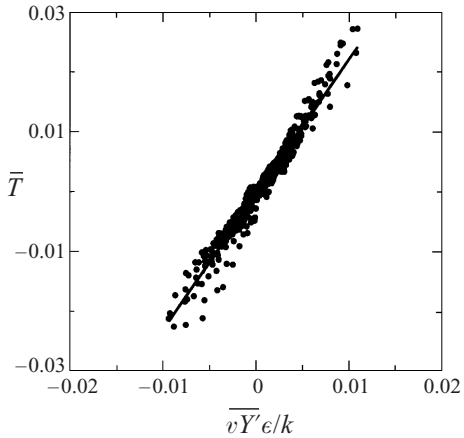


FIGURE 19. Scatter plot of $\overline{T}$ vs. normalized scalar flux across the wake for $t^* > 0.33$ for *Run* 3; regression line slope = 2.3.

regime, C_m approaches a constant ($2 < C_m < 4$). It also appears that the source size does not significantly influence the values of C_m for $t^* > 0.33$. Across the wake (figure 20*b*) away from the centreline and the edges, the values of C_m oscillate between 2 and 4, almost independently of the source size. An average value for C_m across the wake at each time is calculated by replacing $\overline{T}$ and $\overline{vY'}$ in equation (4.15) with the integrals of their absolute values in the y-direction. During the transition from the turbulent convective to the turbulent diffusive regime, C_{mav} exhibits small sensitivity to the source size (figure 20*c*), and has values between 2 and 2.5. For the lower values of Re_0 examined, the time variations of C_{mav} are different from those for the higher Re_0 cases, but no clear trend can be observed. To summarize, it appears that the unconditional PDF method models the scalar flux equation reasonably well after the end of the turbulent convective regime for the highest Re_0 considered. Also, the model prediction is not significantly affected by the source size.

4.3.2. *Scalar variance and dissipation*

The transport equation for the scalar variance provides information about the mechanisms which generate and destroy scalar fluctuations. The scalar variance equation is

$$\frac{\partial(\overline{Y'^2/2})}{\partial t} = \underbrace{-\frac{\partial}{\partial y}(\overline{vY'^2/2})}_{\text{I}} \underbrace{-\overline{vY'}\frac{\partial \overline{Y}}{\partial y}}_{\text{II}} \underbrace{+\frac{1}{Re_0 Sc}\frac{\partial^2}{\partial y^2}(\overline{Y'^2/2})}_{\text{III}} \underbrace{-\overline{\epsilon_Y}}_{\text{IV}}. \tag{4.17}$$

The first term on the right-hand side of equation (4.17) is the turbulent transport of the scalar variance, the second is the production, and the third is the molecular diffusion of the scalar variance. Term IV is the the scalar dissipation,

$$\overline{\epsilon_Y} = \frac{1}{Re_0 Sc}\left(\overline{\frac{\partial Y'}{\partial x_i}\frac{\partial Y'}{\partial x_i}}\right).$$

At the centreline (not shown), the RHS is negative at all times. This is expected after the development time, when the scalar fluctuations decay continuously. Off the centreline (figure 21*a*), at $y^* = -0.52$, the RHS increases from zero to a maximum value, as the wake approaches this point, indicating a continuous increase in the

https://doi.org/10.1017/S0022112000008910 Published online by Cambridge University Press

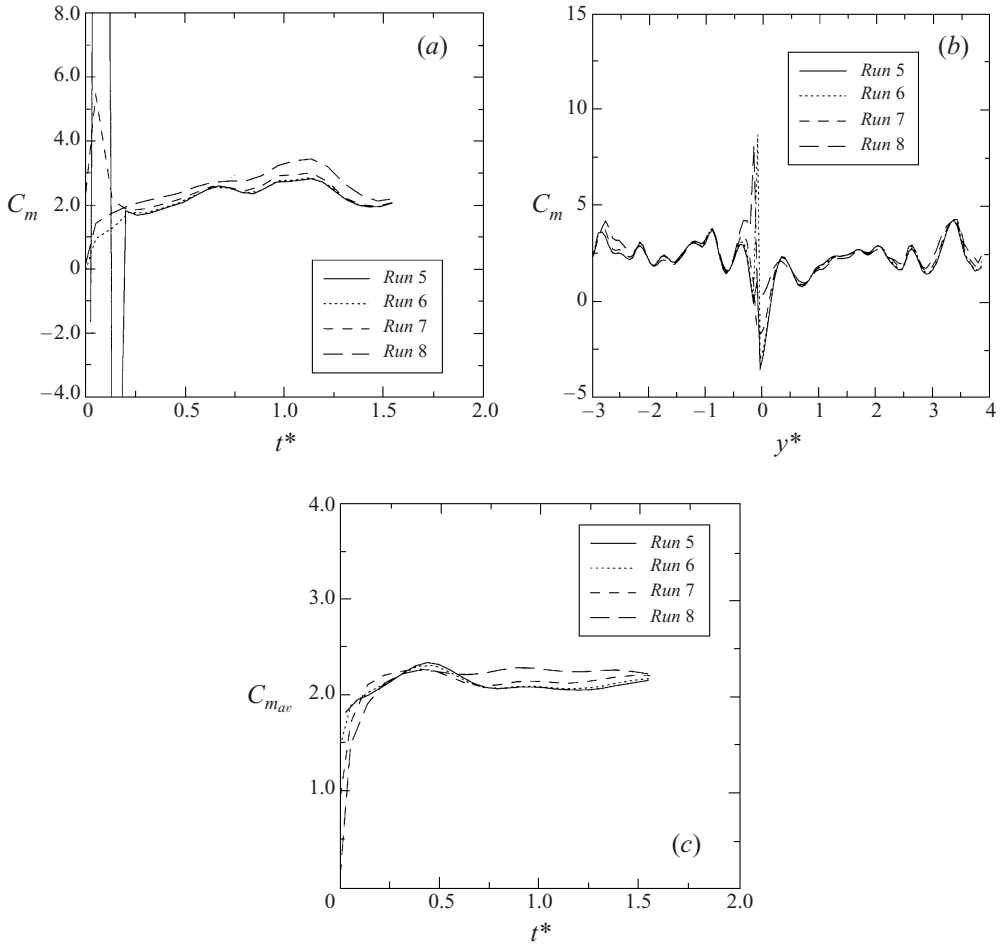


FIGURE 20. (*a*) Time variation of C_m at $y^* = -0.52$, (*b*) y-variation of C_m at $t^* = 1.5$, (*c*) Time evolution of C_{mav}.

scalar variance. Later, the RHS becomes negative and, consequently, the scalar variance starts to decrease. Most of the contribution to the RHS is given at early times by the turbulent transport term, while the production is balanced by the scalar dissipation. Thus, the scalar variance increases due to the turbulent transport from the inner regions of the wake. After the RHS becomes negative ($t^* > 0.4$), the dissipation provides most of the contribution and the production term is balanced by the turbulent transport term. The molecular diffusion term is small at all times, indicating that the scalar variance is transported mainly by the turbulence.

Figure 21(*b*) presents the transversal variation of the terms in equation (4.17) at $t^* = 0.23$. The results agree qualitatively with those of Veeravalli & Warhaft (1990) and are consistent with the above discussion. At the centre of the wake most of the contribution to the RHS is given by the scalar dissipation. As we move away from the centreline, at $y^* = \pm 0.2$ the turbulent transport and the production terms become significant. This is the region where the scalar variance is produced and transported to the outer edges of the wake. Farther from the centreline, for $|y^*| > 0.25$, the RHS becomes positive, indicating that the scalar variance is increasing. In this region, the production term is smaller and it is balanced by the dissipation. Most of the

https://doi.org/10.1017/S0022112000008910 Published online by Cambridge University Press

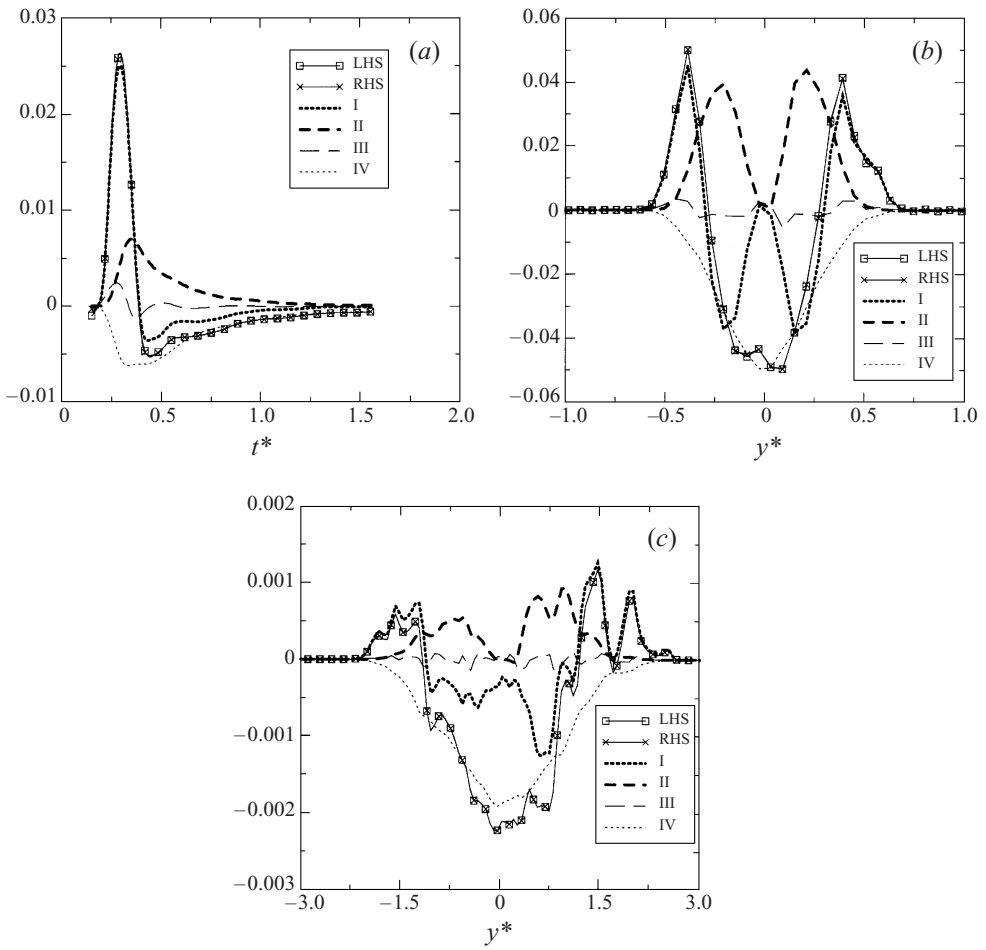


FIGURE 21. (*a*) Time evolution of the terms in scalar variance equation (4.17) for *Run* 3 at $y^* = -0.52$; the terms in the scalar variance equation across the wake at (*b*) $t^* = 0.23$, (*c*) $t^* = 1.0$.

contribution to the RHS is by the turbulent transport term. At the outer edges of the wake ($|y^*| > 0.5$), the most important term in the scalar variance equation is the turbulent transport term. At later times (figure 21*c*), the relative importance of the production and turbulent transport terms decreases in the central region of the wake compared to the dissipation term.

The scalar dissipation is an important term in equation (4.17) at all times. In order to further analyse the small-scale behaviour of the scalar field, as well as the mechanisms responsible for the destruction of the scalar fluctuations, the equation for the scalar dissipation is considered:

$$\frac{\partial \overline{\epsilon_Y}}{\partial t} = \underbrace{-\frac{\partial}{\partial y}(\overline{v\epsilon_y})}_{\mathrm{I}} \underbrace{-\frac{2}{Re_0 Sc}\overline{\frac{\partial Y'}{\partial x_j}\frac{\partial u_i}{\partial x_j}\frac{\partial Y'}{\partial x_i}}}_{\mathrm{II}} \underbrace{-\frac{2}{Re_0 Sc}\frac{\partial \overline{Y}}{\partial y}\left(\overline{\frac{\partial Y'}{\partial x_j}\frac{\partial v}{\partial x_j}}\right)}_{\mathrm{III}}$$
$$\underbrace{-\frac{2}{Re_0 Sc}\frac{\partial^2 \overline{Y}}{\partial y^2}\left(\overline{v\frac{\partial Y'}{\partial y}}\right)}_{\mathrm{IV}} \underbrace{+\frac{1}{Re_0 Sc}\frac{\partial^2 \overline{\epsilon_Y}}{\partial y^2}}_{\mathrm{V}} \underbrace{-\frac{2}{(Re_0 Sc)^2}\left(\overline{\frac{\partial^2 Y'}{\partial x_i \partial x_k}\frac{\partial^2 Y'}{\partial x_i \partial x_k}}\right)}_{\mathrm{VI}}. \tag{4.18}$$

https://doi.org/10.1017/S0022112000008910 Published online by Cambridge University Press

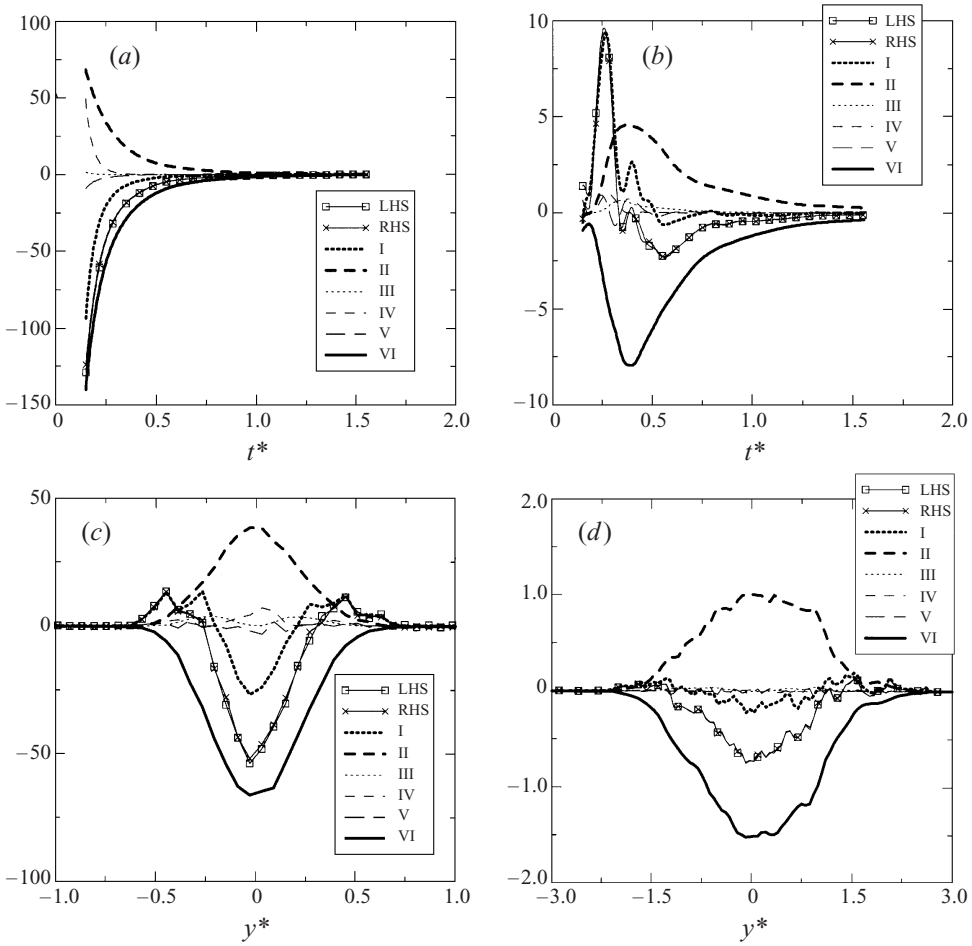


FIGURE 22. Time evolution of the terms in scalar dissipation equation (4.18) for *Run* 3 at (*a*) $y^* = 0.0$, (*b*) $y^* = -0.52$; the terms in the scalar dissipation equation across the wake at (*c*) $t^* = 0.23$, (*d*) $t^* = 1.0$.

The terms in the above equation are: (I) turbulent transport of the scalar dissipation, (II) production by turbulent stretching of the scalar gradient, (III) production by mean scalar gradient, (IV) production by curvature of the mean scalar field, (V) molecular diffusion and (VI) molecular dissipation. At the centreline (figure 22*a*) the time variation of the terms in equation (4.18), after the initial development time, shows a continuous decay of the scalar dissipation. Terms I, II and VI are the main contributors to the RHS. Therefore, the production of the scalar dissipation is primarily due to the stretching of the scalar gradient, while the destruction is due to the molecular dissipation. Off the centreline (figure 22*b*) as the wake reaches $y^* = -0.52$, most of the contribution to the RHS is by the turbulent transport term, while the other terms balance each other. At later times ($t^* > 0.5$), terms I, III, IV and V are less significant and the most important terms are the production by turbulent stretching of the scalar gradient and the molecular dissipation of the scalar dissipation.

To further understand the behaviour of the scalar dissipation, the y-variation of the terms in equation (4.18) is examined. At $t^* = 0.23$, terms I, II, and VI are significant.

https://doi.org/10.1017/S0022112000008910 Published online by Cambridge University Press

The profiles for terms II and VI are single peaked, with the maximum values occurring on the centreline (figure 22*c*). The most important mechanism of producing scalar dissipation in the central region of the wake is the small-scale interaction between the scalar field and the turbulence (term II). The turbulent transport term is negative in the central region and becomes positive towards the outer zone of the wake. This results in a flux of scalar dissipation from the central region of the wake to the outer edges. Thus, the main reason for the increase in the value of scalar dissipation at the outer edges is the turbulent transport from the inner regions of the wake. This is similar to the results obtained for the mean scalar, scalar flux and scalar variance. At later times (figure 22*d*), the turbulent transport term is less significant compared to terms II and VI, except at the outer edges where it becomes important.

The scalar dissipation rate is usually modelled by assuming that the ratio of the time scale of the turbulent energy dissipation and that of scalar variance dissipation,

$$C_Y = \frac{2k/\epsilon}{\overline{Y'^2}/\overline{\epsilon_Y}}, \tag{4.19}$$

is constant. The joint PDF equation (4.12) can be integrated by modelling the terms on the right-hand side, and the scalar variance transport equation can be constructed (Pope 1985). This equation is identical to the exact equation (4.17), except that the scalar dissipation is modelled according to equation (4.19). Thus, both the classical closures and the unconditional PDF method use the same model for the scalar dissipation. Following the turbulent convective regime, the scalar dissipation and the scalar variance become highly correlated ($\zeta(\overline{\epsilon_Y}, \overline{Y'^2}\epsilon/2k) = 0.96$), although the relationship between the two quantities is not linear (figure 23). For larger source sizes, the scatter of the points increases as shown in figure 23, but the correlation remains high even for the largest source size analysed ($\zeta(\overline{\epsilon_Y}, \overline{Y'^2}\epsilon/2k) = 0.92$ for *Run* 8). A value of 2 is usually employed for C_Y (e.g. Anand & Pope 1985), although there is much evidence that it does not take a universal value (Fox 1997). Overholt & Pope (1996) found in their stationary turbulence simulations that C_Y increases with Reynolds number and suggest that it could be flow dependent. The asymptotic value of C_Y should not depend on the source size, but Li & Bilger (1996) suggest that the distance within which C_Y approaches the value of 2 could be a function of the source size.

Figure 24(*a*) shows the time variation of C_Y at the centreline for source sizes ranging from the Kolmogorov microscale to the integral scale. At early times, since the scalar fluctuations are very small, a singularity is obtained in equation (4.19) and C_Y becomes very large. The scalar fluctuations are generated by the presence of the mean scalar gradient and, as a result, the values of C_Y are dependent on the source size at initial times. As the wake develops, the influence of turbulence on the scalar field structure becomes more and more significant and the values of C_Y become less dependent on the source size. Near the end of the simulations C_Y is still decreasing and values between 2.55 for the biggest source and 2.74 for the smallest source are obtained. Similar results are found at $y^* = -0.52$ (figure 24*b*), although it appears that the values of C_Y obtained for the larger scalar sources approach an asymptotic value earlier. Across the wake, the differences between the values of C_Y for different source sizes are small at later times (figure 24*c*). An average value for C_Y is calculated by replacing the values of the scalar dissipation and scalar variance in equation (4.19) with their integrals in the y-direction. The time evolution of $C_{Y\,av}$, presented in figure 24(*d*), is consistent with the above discussion. At the end of the simulations, the

https://doi.org/10.1017/S0022112000008910 Published online by Cambridge University Press

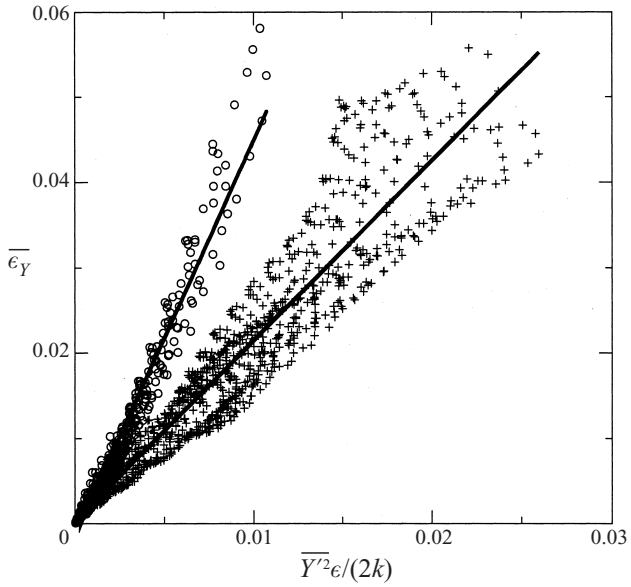


FIGURE 23. Scatter plot of scalar dissipation vs. normalized scalar variance across the wake for $t^* > 0.33$. *Run* 3 (open circles), regression line slope = 4.6. For clarity, the values for both $\overline{\epsilon_Y}$ and $\overline{Y'^2}\epsilon/(2k)$ are magnified 3 times. *Run* 8 (pluses), regression line slope = 2.1.

values of $C_{Y\,av}$ are still decreasing with small differences between the runs. But it also appears that the curves obtained for larger source sizes approach the asymptotic value of 2 earlier.

In order to examine the Reynolds number influence on the time evolution and source size dependence of C_Y, several simulations were performed at lower Re_0 (see § 2.3) using the scalar initialization of *Runs* 5–8. For all the simulations, the scalar fields are generated at the same numerical time as for the corresponding runs with $Re_0 = 350$. Figure 25 presents the time evolution of $C_{Y\,av}$ for different values of Re_0 and the scalar initialization corresponding to *Runs* 5 and 8. The evolution of $C_{Y\,av}$ does not change significantly with Re_0, and for all the values of Re_0 examined, $C_{Y\,av}$ approaches the asymptotic value of 2 earlier for larger source sizes.

5. Summary and conclusions

The present study is concerned with the structure and the development of the scalar wake generated by a single line source in an isotropic decaying turbulent flow. DNS was used to confirm the Warhaft's (1984) experimental results for the velocity and the scalar fields. The numerical and experimental quantities are compared by choosing the appropriate reference scales for length, time and velocity. The time origin was selected by determining the time corresponding to the location of the heated wire in W84. The initial parameters of the velocity field are found by matching the values of Re_λ at all the measurement points. In addition to the base velocity field (which matched the W84 experiment) several other velocity fields were generated for initial Reynolds number $100 < Re_0 < 350$ which resulted in $24 < Re_\lambda < 44$ at the location of the scalar source.

Several initial scalar profiles are examined. The results for the mean and the r.m.s. scalar wakes are in good agreement with W84. Higher-order moments of the scalar

https://doi.org/10.1017/S0022112000008910 Published online by Cambridge University Press

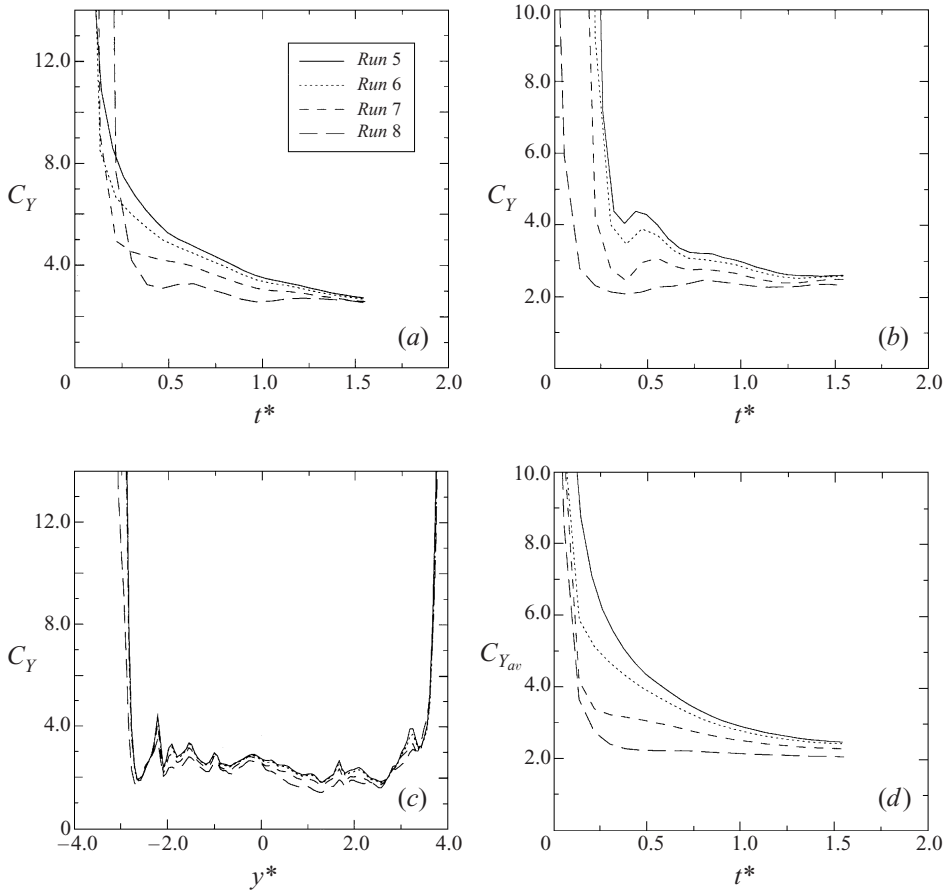


FIGURE 24. Time variation of C_Y at (*a*) $y^* = 0$, (*b*) $y^* = -0.52$, (*c*) C_Y variation across the wake at $t^* = 1.5$. (*d*) Time evolution of $C_{Y\,av}$.

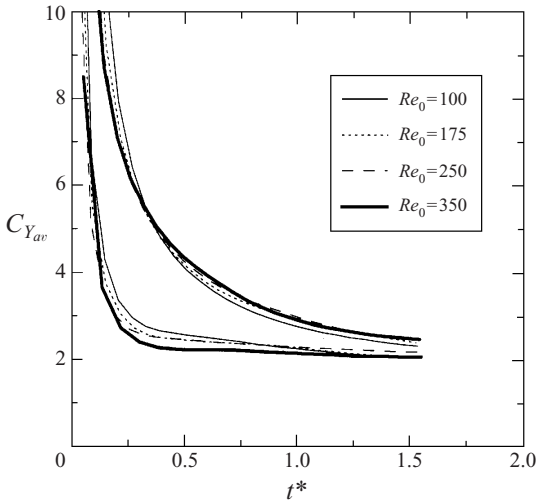


FIGURE 25. Time evolution of $C_{Y\,av}$ for different initial Reynolds numbers. The upper and lower curves correspond to the scalar initializations used for *Runs* 5 and 8, respectively.

https://doi.org/10.1017/S0022112000008910 Published online by Cambridge University Press

PDF have also been calculated. The kurtosis versus skewness of the scalar mass fraction agrees with the experimental results of Mole & Jones (1994) and Li & Bilger (1996) and shows small sensitivity to the Reynolds number for the range of Re_0 examined.

The influence of the scalar source size on the development of the scalar wake is studied for source sizes ranging from the Kolmogorov microscale to the integral scale. After an initial development time, the growth rates of the half-width for the mean and r.m.s. scalar profiles become independent of the initial source diameter. However, for the time period simulated, the scalar intensity on the centreline is dependent on the size and shape of the source.

In order to examine the structure of the scalar wake, the scalar variance is decomposed into a contribution from the flapping of the wake around the centreline and a contribution from the internal structure of the wake. For a source size small compared to the Kolmogorov microscale, during the initial stages of the development the wake behaves like a laminar wake meandering around the centreline. At early times, for the smallest source size analysed, most of the contribution to the scalar variance is from the flapping of the instantaneous wake around the centreline. In the turbulent convective regime, the wake develops internal structure and, near the end of this regime, the flapping component becomes negligible. For larger source sizes, the contribution of the flapping to the development of the scalar wake is less important at all times.

The structure of the scalar wake is further examined by considering the scalar PDF at the centreline of the wake. For the smallest source size studied, the scalar PDF is initially single peaked and becomes double peaked primarily due to the meandering of the wake. As the flapping of the wake weakens, the PDF becomes single peaked again. A similar type of evolution for the scalar PDF is also observed for the largest source size studied. However, for this case it appears that the meandering of the wake is not responsible for the observed double peak in the scalar PDF.

The development of the scalar wake and the mechanisms which contribute to the spreading of the wake are studied by examining in detail the evolution of all the terms in the mean, scalar flux, variance, and scalar dissipation equations. After analysing the exact scalar equations, two types of closures for the mean and scalar variance equations are discussed. During the early stages of the development of the wake, the gradient diffusion and PDF models do not capture the behaviour of the scalar flux and scalar dissipation. Although the correlation between the scalar flux and the mean scalar gradient is high during the transition to the turbulent diffusive regime, the value of Γ_t calculated from DNS data varies across the wake and in time. The average value of Γ_t across the wake increases continuously in time during the simulation, different from the behaviour predicted by the k–ϵ model. The model based on the unconditional PDF method approximates the scalar flux reasonably well during the transition from the turbulent convective to turbulent diffusive regime for the largest Re_0 examined. The initial size of the scalar source does not significantly influence the results obtained for the scalar flux.

The scalar dissipation is usually modelled by assuming that its time scale is proportional to the mechanical dissipation time scale. The same proportionality relation appears in the model based on the unconditional PDF method. Near the end of the simulation, the value of C_Y determined from DNS data is still decreasing, but it appears to approach the theoretical value of 2 obtained for the turbulent diffusive regime. The difference in the values calculated for C_Y for different source sizes decreases in time and becomes small at the end of the simulation. However, the

https://doi.org/10.1017/S0022112000008910 Published online by Cambridge University Press

time evolution of the average value of C_Y across the wake seems to indicate that the asymptotic value is reached earlier for larger source sizes. The initial value of the Reynolds number does not significantly influence the evolution of C_Y for the range of Reynolds numbers examined.

We thank one of the referees for his suggestion of including the Reynolds number dependence of some of the scalar wake quantities presented (e.g. K and C_Y). This work is sponsored by the National Science Foundation under Grant No. CTS-9623178. Computational resources were provided by the San Diego Supercomputer Center, National Center for Supercomputer Applications at the University of Illinois Urbana-Champaign, and the Center for Computational Research at State University of New York at Buffalo.

REFERENCES

Anand, M. & Pope, S. B. 1985 Diffusion behind a line source in grid turbulence. In *Turbulent Shear Flows 4* (ed. L. Bradbury *et al.*), pp. 46–61. Springer.

Buch, K. A. & Dahm, W. J. A. 1996 Experimental study of the fine scale structure of conserved scalar mixing in turbulent shear flows. Part 1. $Sc \gg 1$. *J. Fluid Mech.* **317**, 21–71.

Buch, K. A. & Dahm, W. J. A. 1998 Experimental study of the fine scale structure of conserved scalar mixing in turbulent shear flows. Part 2. $Sc \approx 1$. *J. Fluid Mech.* **364**, 1–29.

Chatwin, P. C. & Sullivan, P. J. 1990 A simple and unifying physical interpretation of scalar fluctuation measurements from many turbulent shear flows. *J. Fluid Mech.* **212**, 533–556.

Durbin, P. A. 1980 A stochastic model of two-particle dispersion and concentration fluctuations in homogeneous turbulence. *J. Fluid Mech.* **100**, 279–302.

Fox, R. O. 1995 The spectral relaxation model of the scalar dissipation rate in homogeneous turbulence. *Phys. Fluids* **7**, 1082–1094.

Fox, R. O. 1997 The Lagrangian spectral relaxation model of the scalar dissipation in homogeneous turbulence. *Phys. Fluids* **9**, 2364–2386.

Givi, P. 1989 Model free simulations of turbulent reacting flows. *Prog. Energy Combust. Sci.* **15**, 1–107.

Givi, P. 1994 Spectral and random vortex methods in turbulent reacting flows. In *Turbulent Reacting Flows* (ed. P. A. Libby & F. A. Williams), Chap. 8, pp. 475–572. Academic.

Givi, P. & Madnia, C. K. 1992 Spectral methods in combustion. In *Numerical Modeling in Combustion* (ed. T. Chung), pp. 409–452. Hemisphere.

Gottlieb, D. & Orszag, S. A. 1977 *Numerical Analysis of Spectral Methods: Theory and Applications.* SIAM, Philadelphia.

Jaberi, F. A., Miller, R. S., Madnia, C. K. & Givi, P. 1996 Non-Gaussian scalar statistics in homogeneous turbulence. *J. Fluid Mech.* **313**, 241–282.

Kerr, R. M. 1985 High-order derivative correlations and the alignment of small-scale structures in isotropic numerical turbulence. *J. Fluid Mech.* **153**, 31–58.

Launder, B. E. & Spalding, D. B. 1972 *Mathematical Models of Turbulence.* Academic.

Leonard, A. D. & Hill, J. C. 1991 Scalar dissipation and mixing in turbulent reacting flows. *Phys. Fluids* A **3**, 1286–1299.

Li, J. D. & Bilger, R. W. 1996 The diffusion of conserved and reactive scalars behind line sources in homogeneous turbulence. *J. Fluid Mech.* **318**, 339–372.

Miller, R. S., Jaberi, F. A., Madnia, C. K. & Givi, P. 1995 The structure and the small-scale intermittency of passive scalars in homogeneous turbulence. *J. Sci. Comput.* **10**, No. 1, 151–180.

Mole, N. & Clarke, E. D. 1995 Relationship between higher moments of concentration and of dose in turbulent dispersion. *Boundary-Layer Met.* **73**, 35–52.

Mole, N. & Jones, C. D. 1994 Concentration fluctuation data from dispersion experiments carried out in stable and unstable conditions. *Boundary-Layer Met.* **67**, 41–74.

Pope, S. B. 1985 PDF methods for turbulent reactive flows. *Prog. Energy Combust. Sci.* **11**, 119–192.

Overholt, M. R. & Pope, S. B 1996 Direct numerical simulation of a passive scalar with imposed mean gradient in isotropic turbulence. *Phys. Fluids* **8**, 3128–3148.

https://doi.org/10.1017/S0022112000008910 Published online by Cambridge University Press

RUETSCH, G. R. & MAXEY, M. R. 1991 Small-scale features of vorticity and passive scalar fields in homogeneous-isotropic turbulence. *Phys. Fluids* A **3**, 1587–1597.

SAWFORD, B. L. & HUNT, J. C. R. 1986 Effects of turbulence structure, molecular diffusion and source size on scalar fluctuations in homogeneous turbulence. *J. Fluid Mech.* **165**, 373–400.

SAWFORD, B. L. & SULLIVAN, P. J. 1995 A simple representation of a developing contaminant concentration field. *J. Fluid Mech.* **289**, 141–157.

SREENIVASAN, K. R., TAVOULARIS, S., HENRY, R. & CORRSIN, S. 1980 Temperature fluctuations in grid-generated turbulence. *J. Fluid Mech.* **100**, 597–623.

STAPOUNTZIS, H., SAWFORD, B. L., HUNT, J. C. R. & BRITTER, R. E. 1986 Structure of the temperature field downstream of a line source in grid turbulence. *J. Fluid Mech.* **165**, 401–424.

TAYLOR, G. I. 1935 Statistical theory of turbulence. *Proc. R. Soc. Lond.* A **151**, 465–478.

THOMSON, D. J. 1990 A stochastic model for the motion of particle pairs in isotropic high-Reynolds-number turbulence, and its application to the problem of concentration variance. *J. Fluid Mech.* **210**, 113–153.

THOMSON, D. J. 1996 The second-order moment structure of dispersing plumes and puffs. *J. Fluid Mech.* **320**, 305–329.

TOWNSEND, A. A. 1954 The diffusion behind a line source in homogeneous turbulence. *Proc. R. Soc. Lond.* A **224**, 487–512.

UBEROI, M. S. & CORRSIN, S. 1952 Diffusion of heat from a line source in isotropic turbulence. *NACA Tech Note* 2710.

VEERAVALLI, S. & WARHAFT, Z. 1990 Thermal dispersion from a line source in the shearless turbulence mixing layer. *J. Fluid Mech.* **216**, 35–70.

WARHAFT, Z. 1984 The interference of thermal fields from line sources in grid turbulence. *J. Fluid Mech.* **144**, 363–387 (referred to herein as W84).

WARHAFT, Z. & LUMLEY, J. L. 1978 An experimental study of the decay of temperature fluctuations in grid-turbulence. *J. Fluid Mech.* **88**, 659–684.

https://doi.org/10.1017/S0022112000008910 Published online by Cambridge University Press